Theses and Dissertations   1. Thesis and Dissertation Collection, all items

2016-12

Transonic axial splittered rotor tandem stator stage

Terrell, Aaron D.

Monterey, California: Naval Postgraduate School

https://hdl.handle.net/10945/51624

NAVAL POSTGRADUATE SCHOOL

MONTEREY, CALIFORNIA

THESIS

TRANSONIC AXIAL SPLITTERED ROTOR TANDEM STATOR STAGE

by

Aaron D. Terrell

December 2016

Thesis Advisor:	Anthony Gannon
Second Reader:	Garth Hobson

THIS PAGE INTENTIONALLY LEFT BLANK.

1. AGENCY USE ONLY *(Leave blank)*	2. REPORT DATE December 2016	3. REPORT TYPE AND DATES COVERED Master's thesis	
4. TITLE AND SUBTITLE TRANSONIC AXIAL SPLITTERED ROTOR TANDEM STATOR STAGE			5. FUNDING NUMBERS
6. AUTHOR(S) Aaron D. Terrell			
7. PERFORMING ORGANIZATION NAME(S) AND ADDRESS(ES) Naval Postgraduate School Monterey, CA 93943-5000			8. PERFORMING ORGANIZATION REPORT NUMBER
9. SPONSORING /MONITORING AGENCY NAME(S) AND ADDRESS(ES) N/A			10. SPONSORING / MONITORING AGENCY REPORT NUMBER
11. SUPPLEMENTARY NOTES The views expressed in this thesis are those of the author and do not reflect the official policy or position of the Department of Defense or the U.S. Government. IRB number _____N/A_____.			
12a. DISTRIBUTION / AVAILABILITY STATEMENT Approved for public release. Distribution is unlimited.			12b. DISTRIBUTION CODE

13. ABSTRACT (maximum 200 words)

   Development of a procedure to model the hot shape of a rotor blade and a comparison analysis of the transonic axial splittered rotor (TASR), tandem stator (TS) stage has been investigated. The ability to implement this procedure into the current Naval Postgraduate School (NPS) Turbopropulsion Lab (TPL) design procedure that uses commercial off the shelf software has been documented. The TS stage was tested at multiple clocking positions over the full speed range of the rotor. The best performance was observed at a negative 10 percent clocking position relative to the design configuration. Numerical simulations were conducted of both hot and cold rotor shapes and compared.

   This study advanced the understanding of simulating the hot shape of a rotor to better match the results of experimental data. The hot shape results closely resembled that of the cold shape results; however, the hot shape achieved a greater mass flow range. The procedure developed is easily implemented, utilizing a fluid-structure interaction. Rotational forces as well as gas loading forces were observed as an influence on blade deformation. Utilizing the procedure to model the hot shape of the rotor will be essential in deriving numerical results for a comparative analysis.

14. SUBJECT TERMS Turbomachinery, splittered rotor, tandem stator, transonic compressor, blade deformation, fluid-structure interaction			15. NUMBER OF PAGES 87
			16. PRICE CODE
17. SECURITY CLASSIFICATION OF REPORT Unclassified	18. SECURITY CLASSIFICATION OF THIS PAGE Unclassified	19. SECURITY CLASSIFICATION OF ABSTRACT Unclassified	20. LIMITATION OF ABSTRACT UU

i

THIS PAGE INTENTIONALLY LEFT BLANK.

TRANSONIC AXIAL SPLITTERED ROTOR TANDEM STATOR STAGE

Aaron D. Terrell
Lieutenant, United States Navy
B.S., United States Naval Academy, 2010

Submitted in partial fulfillment of the
requirements for the degree of

MASTER OF SCIENCE IN MECHANICAL ENGINEERING

from the

**NAVAL POSTGRADUATE SCHOOL
December 2016**

Approved by: Anthony Gannon
Thesis Advisor

Garth Hobson
Second Reader

Garth Hobson
Chair, Department of Mechanical and Aerospace Engineering

THIS PAGE INTENTIONALLY LEFT BLANK.

ABSTRACT

Development of a procedure to model the hot shape of a rotor blade and a comparison analysis of the transonic axial splittered rotor (TASR), tandem stator (TS) stage has been investigated. The ability to implement this procedure into the current Naval Postgraduate School (NPS) Turbopropulsion Lab (TPL) design procedure that uses commercial off the shelf software has been documented. The TS stage was tested at multiple clocking positions over the full speed range of the rotor. The best performance was observed at a negative 10 percent clocking position relative to the design configuration. Numerical simulations were conducted of both hot and cold rotor shapes and compared.

This study advanced the understanding of simulating the hot shape of a rotor to better match the results of experimental data. The hot shape results closely resembled that of the cold shape results; however, the hot shape achieved a greater mass flow range. The procedure developed is easily implemented, utilizing a fluid-structure interaction. Rotational forces as well as gas loading forces were observed as an influence on blade deformation. Utilizing the procedure to model the hot shape of the rotor will be essential in deriving numerical results for a comparative analysis.

THIS PAGE INTENTIONALLY LEFT BLANK.

TABLE OF CONTENTS

LIST OF FIGURES

x

LIST OF TABLES

THIS PAGE INTENTIONALLY LEFT BLANK.

LIST OF ACRONYMS AND ABBREVIATIONS

AS	Axial Segment
CFD	Computational Fluid Dynamics
CFX	The CFD simulation program in ANSYS Workbench. It is divided into CFX-Pre, CFX-Solver, and CFX-Post. It uses an implicit solver and can run both steady-state and transient simulations.
FSI	Fluid-Structure Interaction
HPVEE	Hewlett-Packard Visual Engineering Environment
LB	Lead Blade
LE	Leading Edge (blade)
MB	Main Blade
NPS	Naval Postgraduate School
PLA	Polyactic Acid
SB	Splitter Blade
SS	Static Structural
SW	SolidWorks (a solid modeling program)
TASR	Transonic Axial Splittered Rotor
TB	Trail Blade
TCR	Transonic Compressor Rig
TE	Trailing Edge (blade)
TS	Tandem Stator
TPL	Turbopropulsion Lab

THIS PAGE INTENTIONALLY LEFT BLANK.

ACKNOWLEDGMENTS

First and most importantly, I want to thank my wife, Angela, for allowing me the time to complete postgraduate school. Many thanks to Dr. Gannon for the insight and encouragement that propelled me forward. As busy as a department chair can be, Dr. Hobson was always willing to answer any questions and ensure I was pointed in the right direction. John Gibson has the ability look at a problem and make it go away; thank you for all the help you provided. Andria Holmes, thank you for our weekly sports discussions and all the help you provided. Dr. Platzer, thank you for sharing your experiences with me. Sabine Bauinger, thank you for all your help with experimental practices and for explaining everything Dr. Gannon said to me three or four more times. Last, I want to thank all my fellow master's students. I could not have made it through the classes or completed this thesis without your help.

THIS PAGE INTENTIONALLY LEFT BLANK.

I. INTRODUCTION

A. MOTIVATION

Studies conducted at the Naval Postgraduate School (NPS) Turbopropulsion Laboratory (TPL) have identified a design process for axial compressor rotors accompanied with an adjustable tandem stator. The compressor rotor was designed incorporating a splitter vane between the principal blades. Historical experiments conducted by Dr. Arthur J. Wennerstrom [1] identified success using splitter vanes in compressors. The results showed major increases in loading capability and efficiency. This finding was significant for future designs to continue the incorporation of splitter vanes. Higher loading of compressor stages allows for a lower total number of stages to achieve an overall higher pressure ratio. Due to a lower number of total stages the machine is lighter, smaller, and at a lower material cost [1]. The high loading capability that was achieved came at the cost of mass flow range, which was significantly reduced, from a conventional rotor design.

The stage is composed of the rotor and stator. The flow of the air passing through the rotor is turned, and the flow is required to be turned to a different direction in order to be passed through the next stage. The stator does the turnaround for the next stage. The goal of stator design is to make this turn with minimal negative affect on the performance of the rotor. The designed stator is a tandem stator that is adjustable to test different clocking positions between the leading blade (LB) and trailing blade (TB).

B. PREVIOUS WORK

1. Wennerstrom Axial Compressor Incorporating Splitter Vanes

Dr. Wennerstrom at the Aero Propulsion Laboratory, Air Force Wright Aeronautical Laboratories, Wright-Patterson Air Force Base, OH, led a research team between 1970 and 1974. During that time, Wennerstrom's team designed and tested ten variants of a supersonic axial compressor stage [2]. One of the test sets was a redesign to a previously designed and tested rotor that exhibited poor performance. The new design introduced a splitter vane "to gain better control of rotor outlet flow angles without

simultaneously reducing throat area and causing significant increases in diffusion losses and weight" [3].

Geometry and placement of the splitter vane were decided on the basis of engineering judgment. Wennerstrom [3] admits, "It might be possible to do a credible job of optimizing splitter-vane geometry analytically by one of the time-dependent or finite element cascade analysis methods… However, at the time of this design… neither the opportunity nor the time was available." Wennerstrom [3] described the placement of the splitter blade, "The splitter vane leading edge was placed halfway, measured axially, between the leading and trailing edge planes of the principal blades. The splitter vane trailing edges lie in the same plane as the trailing edges of the principal blades. The splitter vanes were circumferentially positioned midway between the principal blades." Wennerstrom [3] states, "This is not necessarily an optimum position. However, there was insufficient justification for picking any other location." The design of this rotor was described in detail by Wennerstrom and Frost [3], and Figure 1 is a cascade view of the rotor incorporating splitter vanes. Figure 2 is a projected view of Wennerstrom's rotor incorporating splitter vanes.
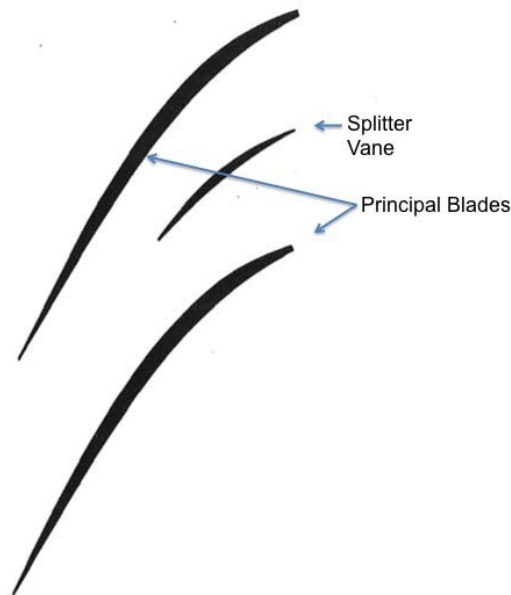
Figure 1. Cascade View of Wennerstrom's Rotor with Splitter Vanes.
Source: [3].
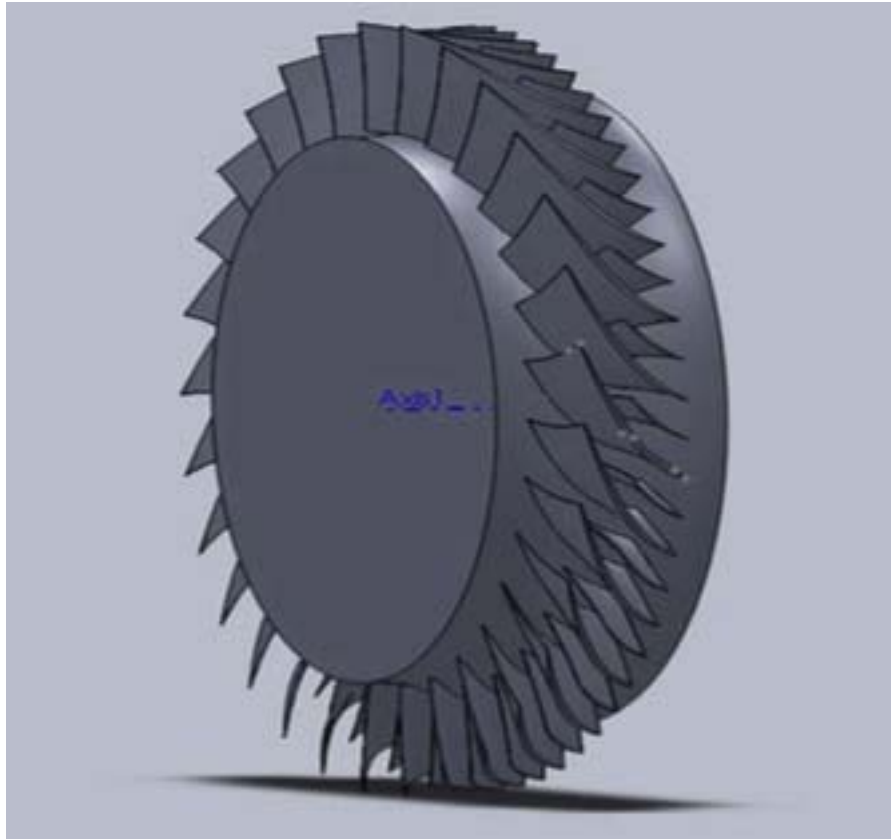
Figure 2. Wennerstrom's Supersonic Axial Rotor with Splitter Vanes.
Source: [4].

The performance of the rotor at design speed attained an experimentally measured 3.47 peak total pressure ratio and 85 percent peak total isentropic efficiency. These achievements are downplayed by the fact of a narrow mass flow rate of 3 percent.

2.   Drayton Transonic Axial Splitter Rotor

The TPL went through multiple design iterations in the design of Transonic Axial Splitter Rotor (TASR). Initiation of the project was performed by Scott Drayton [4] and documented in his dissertation of September 2013. Drayton's tests were conducted as rotor only experiments as opposed to Wennerstrom's stage experiments. Detailed

information about the design tools used as well as the constraints and goals that drove the design are explained in Drayton's dissertation [4].

Drayton's design phase produced a novel procedure capable of completing a numerically derived constant speedline of the rotor's performance to be analyzed and compared to identify design goal achievement. Utilizing this design procedure it was easy to predict rotor performance and adjust the rotor geometry as needed. Four iterations of design and numerically derived results achieved the best blade geometry for design continuation. The best circumferential and axial placement for the splitter blade was identified following a couple more iterations. Figure 3 shows the resulting TASR from Drayton's design phase [4].
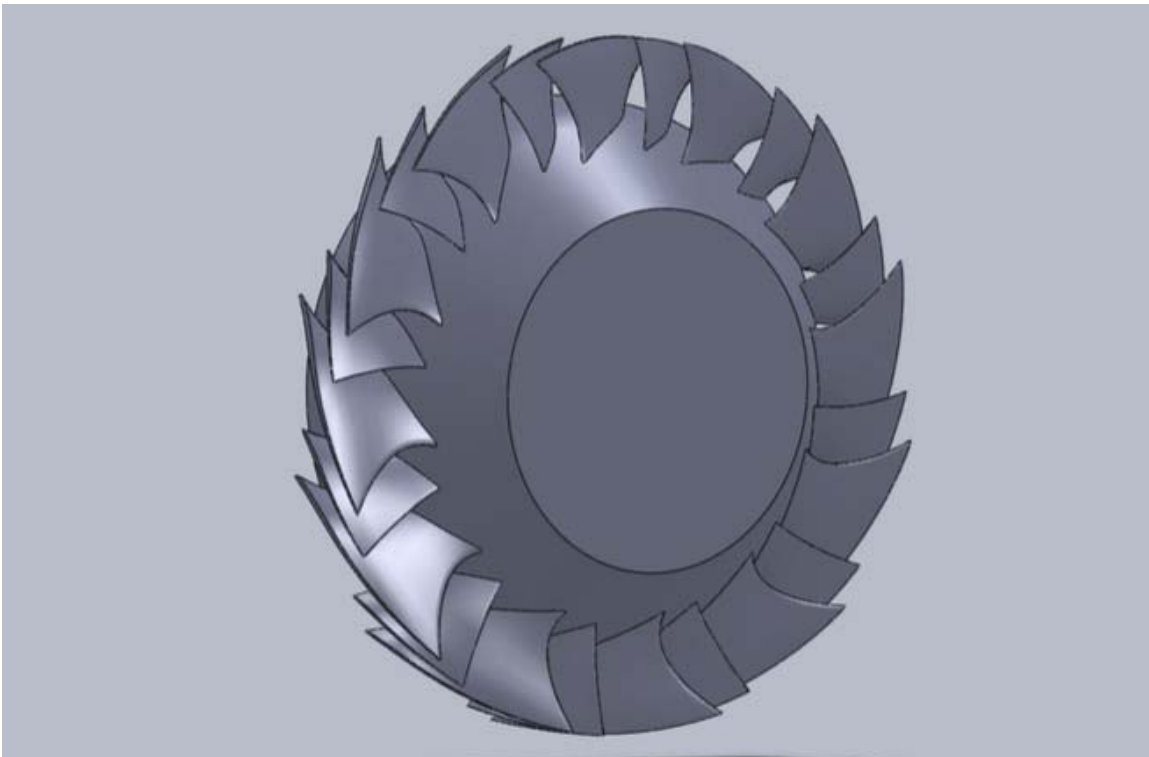
Figure 3. Drayton's TASR. Source: [4].

The splitter blade (SB) chord length was set to be 50 percent of the main blade (MB) chord length. The axial placement of the SB was set at 5.08 mm (0.2 in) forward of the center plane bisecting the MBs axially. The circumferential placement of the SB was

set at 35 percent of the distance spanning from MB to the next MB. At 100 percent design speed and 0.9144 mm (0.036 in) tip gap, TASR achieved a measured peak pressure ratio of 1.69 and an efficiency of 72 percent with a mass flow range of 7.5 percent.

3. Lehrfeld's TASR Adjustable Tandem Stator Combination

The follow on to Drayton was Lehrfeld's [5] work to complete the stage design and is documented in his thesis of December 2013. Lehrfeld incorporated a TS to complete the stage for the compressor. Figure 4 is a SolidWorks (SW) assembly of Drayton's TASR and Lehrfeld's TS. He used the same design procedure with alterations to identify the best geometry and placement of the stator blades.
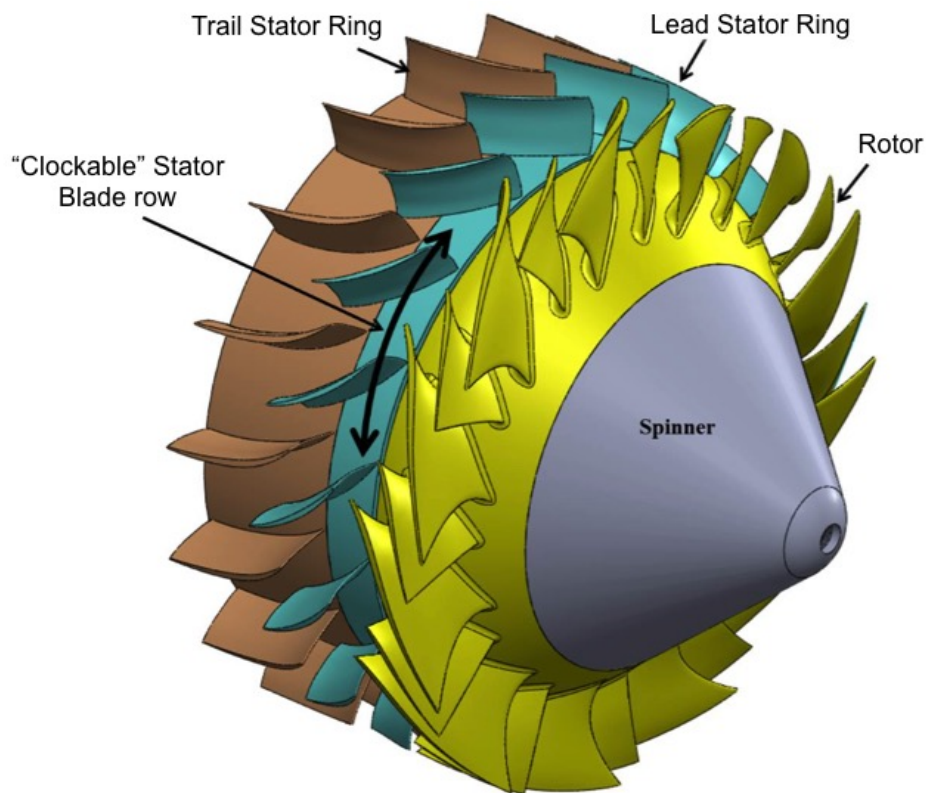
Figure 4. SW Assembly of Drayton's TASR and Lehrfeld's TS. Source: [5].

The stator was designed specifically for the TASR in that the stator initial blade geometry began by matching the rotor exit plane flow angles to the LB's leading edge (LE) angle within the incident flow. Lehrfeld then altered the LB stagger angles to manipulate the blade camber. His goal was to turn the flow axially and at the same time minimize flow separation on the suction side of the LB. The circumferential offset between the LB and TB proved to be important in the design process of the stator. Lehrfeld identified the offset was initially to ensure there was sufficient spacing between the LB and TB; however, after "subsequent iterations it was discovered there was value to varying the blade offset to produce a local aerodynamic throat that would reenergize the flow and produce a delay in flow separation." [5]. Lehrfeld's last design consideration was the incorporation of blade bowing. Lehrfeld [5] explains the concept of blade bowing, "blade bowing counters boundary layer build up and blade corner region interaction by a dihedral or lean angle between the blade and hub and/or casing. The corner interaction regions are the areas where either the LB or the TB meets with the hub or casing." Lehrfeld's design has blade bowing to incorporate a dihedral at the hub and casing.

Lehrfeld's final tandem stator design and the numerical results are paraphrased here. The chord length for the LB was set to 50.8 mm (2 in) and the TB was set to 63.5 mm (2.5 in). There was an overlap of the TB LE and LB trailing edge (TE) of 12.7 mm (0.5 in). The lead stator ring can be clocked to a different setting for testing purposes. The trailing stator ring remains stationary when clocking the lead stator ring and has the entire TB affixed. Lehrfeld did not get the opportunity to physical test his TS; however, he did predict the off-design performance of the stage. At 100 percent design speed and no tip gap, TASR/TS stage achieved a computed maximum peak pressure ratio of 1.97 and an efficiency of 77.5 percent with a mass flow range of 8.4 percent.

C. CURRENT STUDY

The objective of this study is to experimentally determine the performance of the TASR/TS stage at various stator clocking positions. The intent is to verify the numerically determined optimum circumferential relationship between the stator leading

blade and trailing blade. As well as, develop a procedure to capture the hot shape of a rotor and incorporate the hot shape into the TPL's design process. A secondary objective was to determine the effect of two different turbulence models used in the prediction of rotor-only performance.

THIS PAGE INTENTIONALLY LEFT BLANK.

II.   EXPERIMENTAL FACILITY AND PROCEDURES

The TASR/TS stage was tested in the Transonic Compressor Rig (TCR) facility at the NPS TPL. Dr. M. H. Vavra designed the TCR facility; however, modifications to the original design were necessary to accommodate Drayton's TASR design, and further modifications were necessary to accommodate Lehrfeld's TS design. These modifications are described in Drayton [4] and Lehrfeld [5]. This study utilized both the rotor-only set up and the stage set up for the TCR. This chapter summarizes the TCR configuration for the TASR and TS, as well as, the experimental procedures followed for data collection, data acquisition and reduction methods.

A.   TRANSONIC COMPRESSOR RIG CONFIGURATION

Figure 5 is the TCR configuration. Describing from left to right through the TCR, air is drawn into the intake plenum from the atmosphere and passes through multiple screens to capture foreign object debris as well as condition the flow. An electric throttle is an electromechanical actuated rotating plate throttle valve that is manipulated during testing to restrict mass flow and increase loading on the compressor. The electric throttle separates the intake plenum from the settling chamber. The air passes through a flow rate nozzle just after the settling chamber at which point mass flow rate is measured.
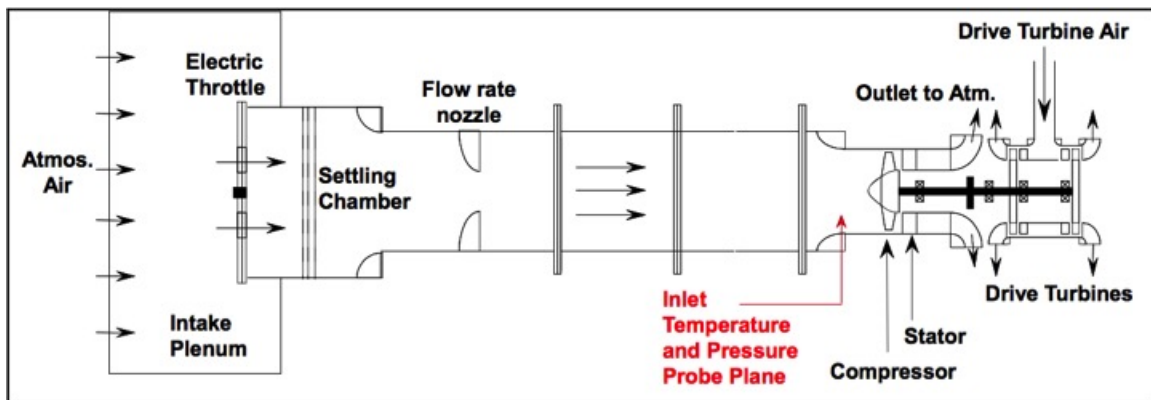
Figure 5. Transonic Compressor Rig. Source: [6].

Then the air passes through 4.2672 m (14 ft) of 0.4572 m (18 in) diameter piping to the test compressor. Once the air is passed through the test compressor it is exhausted to atmosphere. Driving the test compressor are two opposed, single stage air-operated drive turbines. These drive turbines are mounted on a single shaft, as seen on the right side of Figure 5.

The overall configuration of the TCR does not change between different compressors to be tested. The only section that changed was the compressor test section. The following two sections discuss the specific configurations in the test compressor portion of the TCR that were studied.

1.   TASR (Rotor Only) Configuration

A detailed discussion for the installation of the TASR into the compressor test section is in Drayton [4] with design modifications in Lehrfeld [5]. Surrounding the TASR are three rings, these three rings are termed as axial segments (AS) and together make AS1, AS2, and AS3. Numbered from the upstream direction where the flow of air is coming from as seen in Figure 6. These three rings are holed where sensor instrumentation can be placed. AS1 contains the inlet temperature and pressure sensors, AS2 contains the casing transient pressure sensors, and AS3 contains the outlet temperature and pressure sensors. In this study none of the AS2 sensor instrumentation was used. The holed sensor entry areas were taped off so no air could escape the test compressor in this section
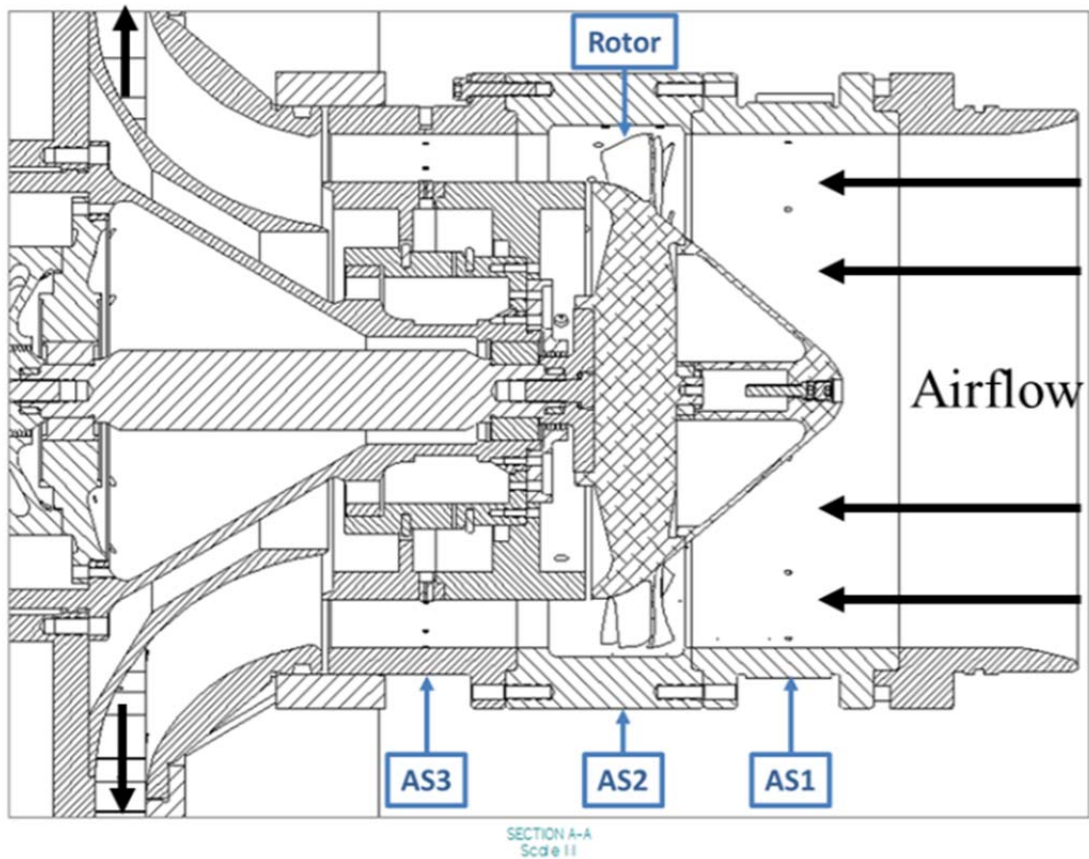
Figure 6. Test Section of the TCR with TASR Configuration. Source: [5].

In the rotor only configuration the air flows between AS3 and blank rings. These rings were a redesigned feature for the TCR when the TS was designed. These rings were fastened to the stator support structure, which was necessary to be in the TCR in the stage configuration. Figure 7 shows the stator support structure.

Figure 7. Stator Support Structure. Source: [5].

2.   **TASR and TS (Stage) Configuration**

The stage configuration removed the blank rings and the lead and trail stator rings are affixed to the stator support structure. The trail stator ring was placed in the assembly first then the lead stator ring was set to a desired clocked position then secured. Once the TS was placed in the compressor test section the rotor was installed. Figure 8 depicts the stage configuration with notations to identify specific components.
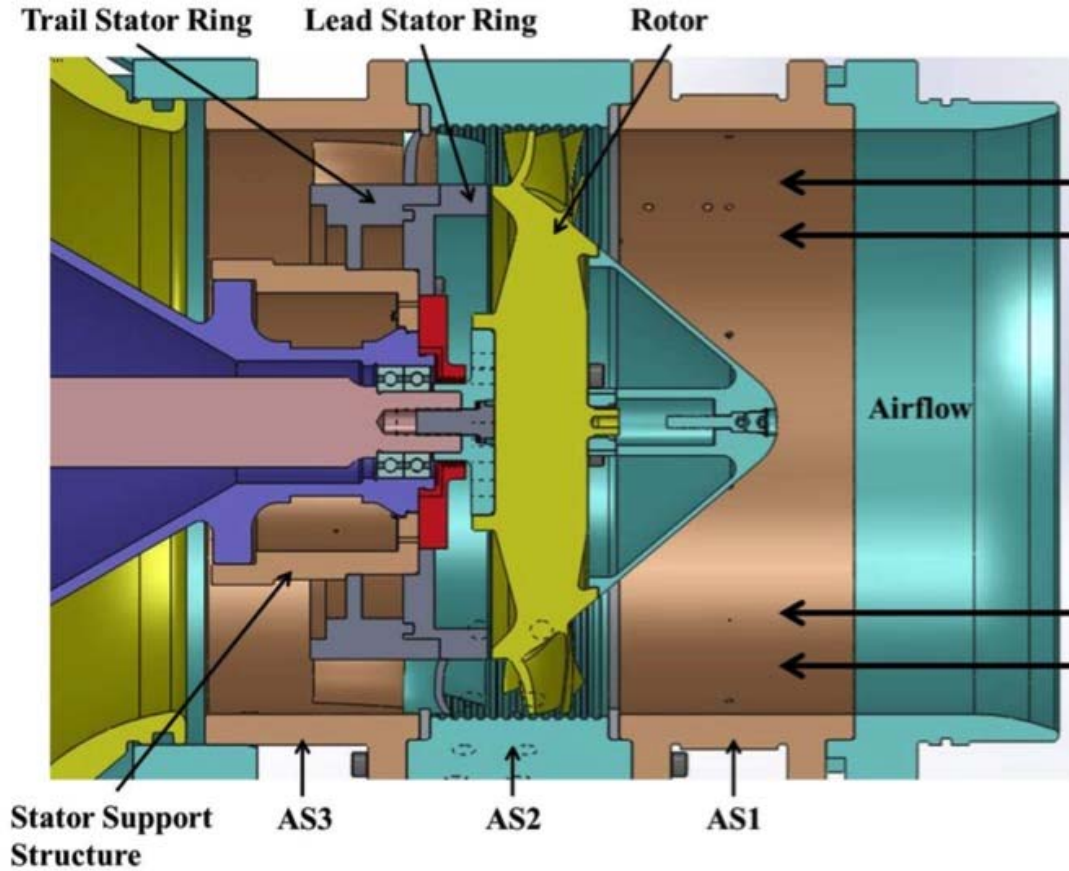
Figure 8. Test Section of the TCR with TASR and TS Stage Configuration.
Source: [5].

Lehrfeld generated 11 different air wedges, each with a different stator setting. The settings ranged from minus 30 percent to plus 30 percent. The percentage is based on distance between two blades of the lead stator ring. Figure 9 is a cascade view of a LB and a TB and shows the positive and negative perturbation the TB can be set to relative to the leading blade [5].
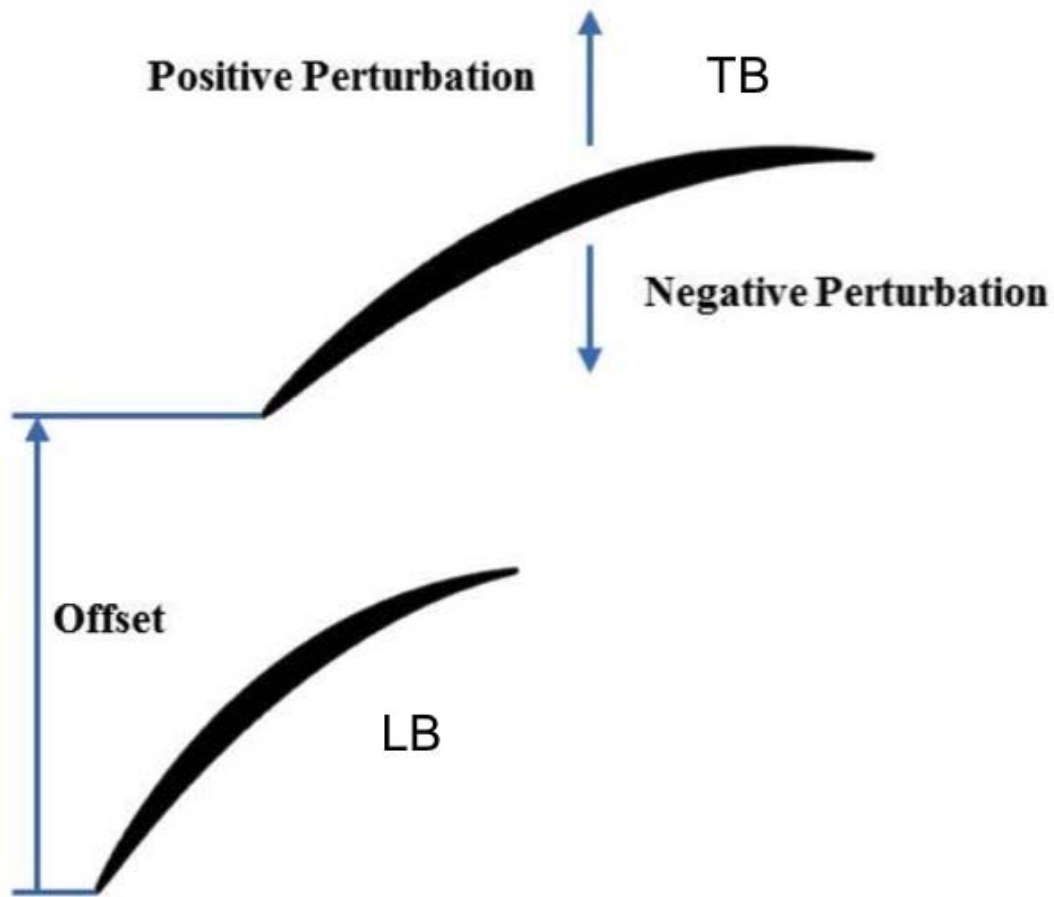
Figure 9. TS Offset Perturbation. Source: [5].

a.   *Development of the Set Tool*

The TS was not manufactured with setting indications or any markings to set the appropriate clocked position. A set tool was needed to test desired clocked positions. Considerations taken into account when deciding a means for designing the set tool were ease of production and ability to replicate the exact settings Lehrfeld designed. The final decision was to take the original parasolid air wedges and cut away sections in SW to form a setting tool mold. Once the air wedges were cut down in SW they were converted to an .stl file to be 3-D printed. The first concern for printing the setting tools was if the print would be able to build up on itself. A proof of concept was undertaken to print the

stator portion of the air wedge. Figure 10 shows this 3-D print of the baseline setting air wedge for the TS section of the compressor.
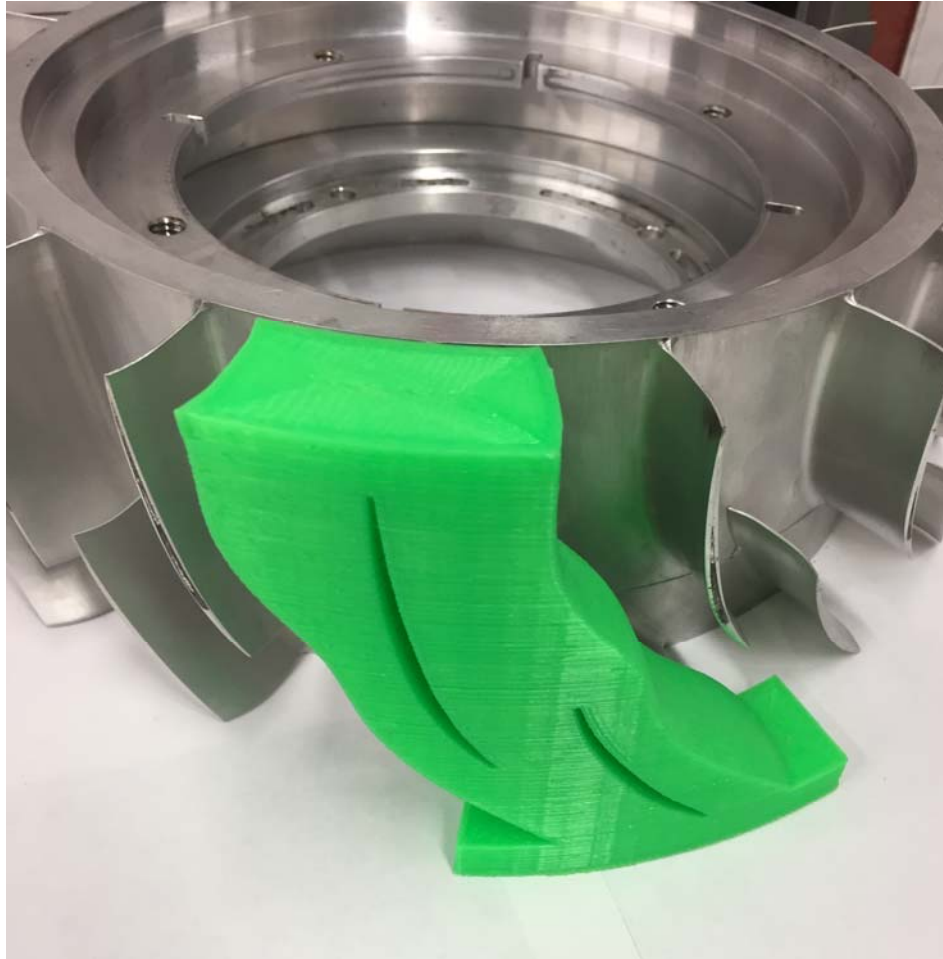
Figure 10. Baseline Setting of TS Air Wedge.

Once the print was in hand and compared next to the TS it was observed that the bowing in the blades of the stator would not allow for the set tool to simply slide over the blades, also this would be impossible because the trail stator ring was locked into place and covered by the casing. The generation of a set tool that could be slid into place from the front was required. Another observed flaw of the first print included the absence of a chamfer that is required for the set tool to slide over a fillet radius surrounding the blade base where it meets the hub. To get the set tool to slide in between the blades of the TS a considerable amount of material had to be cut away from the solid models. Losing the

material decreased the amount of contact surface with the blades and a concern that the tool would be unstable while attempting to set the lead stator ring position needed to be addressed. This concern was overcome by repeating the set tool circumferentially where it would engage multiple blade passages. This would allow for multiple contact surfaces even at the loss material for the front sliding set tool. The second iteration of the set tool took the observations identified into account and was printed. Figure 11 shows the baseline set tool as a SW solid model and the printed tool. Additional cuts made after the model was printed in order to insert the tool through the passage to contact the blade surfaces.
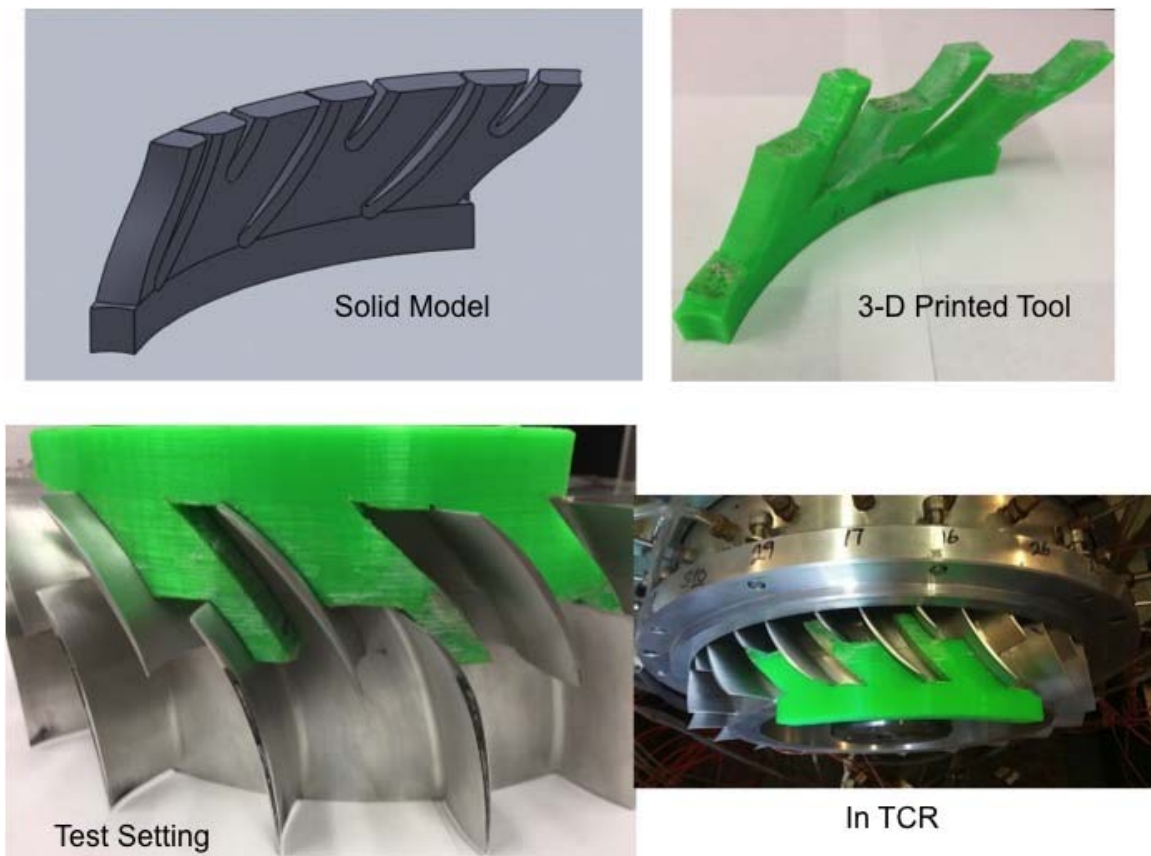
Figure 11. Baseline Set Tool.

Six set tools were made for use in this study. Figure 12 shows the six different set tools. The set tools clock the stator to both negative and positive perturbations from the

16

baseline design. Negative perturbations include 10 and 20 percent offsets. Positive perturbations include 10, 30, and 50 percent offsets.
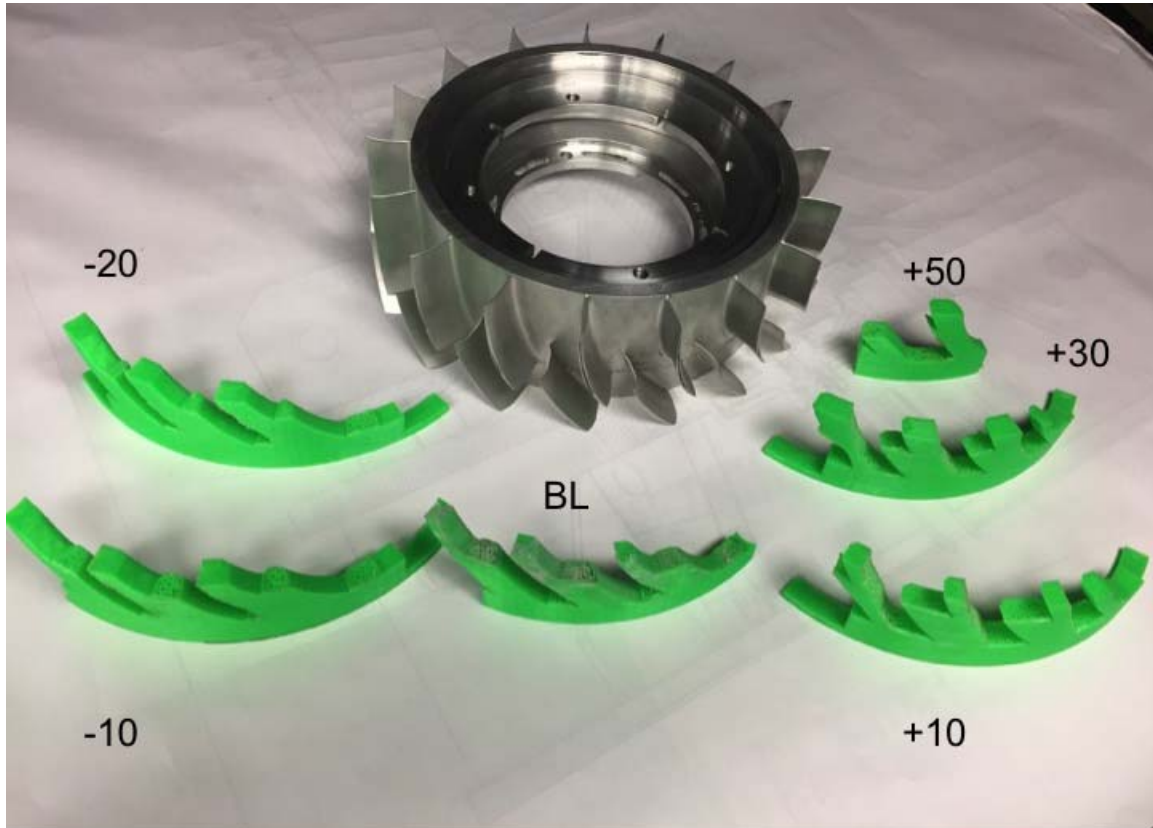
Figure 12. TS Set Tools.

b.   *Glacier Summit—Dual Head Printer*

The set tools were printed using a Glacier Summit—Dual Head Printer shown in Figure 13. The basic movements of the printer are set up in Cartesian coordinates and are manipulated by motors and drive belts. The bed is capable of moving in both the X and Y direction and the extruder is capable of moving in the vertical Z direction. The extruder works in the same manner as a hot glue gun tip. Electrical coils heat the tip of the extruder and melt the plastic filament. The filament is passed through two wheels, one a motor driven wheel, and fed to the extruder.

Bed temperature was altered numerous times in order to maintain consistent contact between the bed surface and the part. Low temperatures allowed the base of the part to completely harden. As the base hardened the internal stresses within the part would relax causing distortion. The distortion of the part would curl the ends upward causing poor contact which caused the part to displace as the bed traversed.
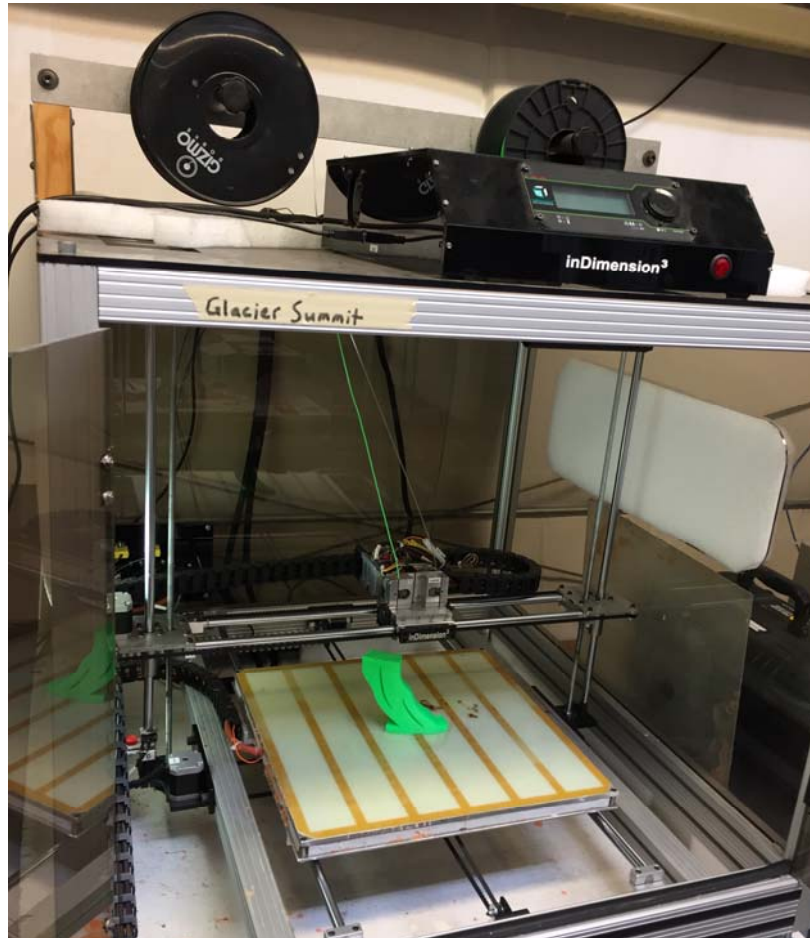
Figure 13. Glacier Summit—Dual Head Printer.

High temperatures caused the base of the part to be too soft. A soft base would not keep its form while the part built up vertically. This problem was not evident until the part was half to three-quarters complete. It is observed from Figure 13 that on the left side of the part, there is significant over hang. Executed prints with too high of a bed temperature would fail when the print reached these areas.

Feed rate and flow rate were two other characteristics of the printer that required numerous adjustments. Flow rate is the speed the material is passed through the extruder. Flow rate settings are governed by the type and thickness of the material. This information is entered into the program and a default flow rate is set. However, the flow rate can still be adjusted to the users preference. Feed rate is the overall speed that the material is laid to the bed. This incorporates the bed traversing speed in both X and Y directions as well as the flow rate. This characteristic was a final tuning function while printing the set tools. The initial layers required a slow feed rate for the material to have sufficient time to stick to the bed. Once the base of the part was formed the feed rate was allowed to increase. Print time averaged to about six hours per set tool.

c.   *Material*

Polyactic acid (PLA), shown in Figure 14, was the material used to make the set tools. This material was selected due to its usefulness in a broad range of printing applications. PLA has the following recommended print settings: extruder temp between 180 and 220 degrees Celsius and bed temperature between 20 and 55 degrees Celsius. The material used has a 1.75 mm diameter.

Figure 14. PLA Spool.

19

d. *Repetier and Slic3r Software*

The two software programs used for 3D printing are Repetier and Slic3r. Repetier is the user interface for setting up and executing the print. Slic3r is an embedded software program within Repetier that takes the user preferences designated in Repetier and translates to a G-code for the encoder to process. The SW files mentioned in subparagraph *a* of this section were saved as a .stl file. This file was transferred to the Repetier software and printer configuration preferences were entered. A detailed list of the configuration preferences are presented in Appendix A.

3.   Experimental Instrumentation

This study used the same type of steady-state probes used by Drayton [4] and Lehrfeld [5]. The probes were 1.59mm (1/16 in) "miniature head" Kiel probes (United Sensor KAA-8) and 3.18 mm (1/8 in) "standard head" combination Kiel/thermocouple probes (United Sensor HT-8J-12-C). Those steady-state probes collected stagnation pressure and temperature in the flow field. Pressure probes in the casing and hub took unsteady static pressure measurements.

4.   Instrument Placement

Instrument placement for this study was done in the same way as Drayton [4]. Drayton explains the instrument placement in his dissertation and is quoted here.

> Inlet measurements were taken in AS1 using four sensors. Two sensors were the Keil/thermocouple probes and the other two were static pressure ports. Outlet measurements were taken in AS3 using 28 sensors. These sensors included eight Keil/combination probes, 12 Keil pressure probes, four static pressure ports in the hub, and two static pressure ports in the casing. Two custom temperature probes were also in AS3 to measure the hub and casing temperature. [4]

Table 1 shows all installed instrumentation used during this study.

Table 1.　TCR Instrumentation.

Port #	Scanivalve 1	Depth (P)	Depth of TC	Depth (T) in [%]	Angle position	Orientation, Rotor only	Temp Channels
1	Tare						
2	Scale						
3	Flow Nozzle P6						
4	Flow Nozzle Ps						
5	Inlet Pt1 Kiel Probe/TC Combo						
6	Inlet Pt1 Kiel Probe/TC Combo						
7	Inlet Ps1 (static)						
8	Inlet Ps1 (static)						
9	Outlet Ps3 (static)				43.2°		
10	Outlet Ps3 (static)				216°		
11	Kiel Probe	0.05	-		0°	0	
12	Kiel Probe	0.1	-		187.2°	0	
13	Kiel Probe	0.2	-		57.6°	0	
14	Kiel Probe	0.25	-		14.4°	0	
15	Kiel Probe	0.3	-		28.8°	0	
16	Kiel Probe	0.35	-		259.2°	0	
17	Kiel Probe/TC combo	0.4	0.05	95.3%	244.8°	0	08
18	Kiel Probe/TC combo	0.45	0.1	90.6%	201.6°	0	07
19	Kiel Probe	0.5	-		331.2°	0	
20	Kiel Probe/TC combo	0.55	0.15	85.8%	86.4°	0	06
21	Kiel Probe	0.6	-		72°	0	
22	Kiel Probe/TC combo	0.65	0.25	76.4%	115.2°	0	05
23	Kiel Probe	0.7	-		288°	0	
24	Kiel Probe/TC combo	0.75	0.35	66.9%	345.6°	0	04
25	Kiel Probe	0.8	-		100.8°	0	
26	Kiel Probe/TC combo	0.85	0.45	57.5%	273.6°	0	03
27	Kiel Probe	0.9	-		158.4°	0	
28	Kiel Probe/TC combo	0.95	0.6	43.3%	172.8°	0	09
29	Kiel Probe	1.0	-		230.4°	0	
30	Kiel Probe/TC combo	1.05	0.7	33.9%	316.8°	0	02
35	Hub static pressure P3 1						
36	Hub static pressure P3 2						
37	Hub static pressure P3 3						
38	Hub static pressure P3 4						
49	Custom temperature probe		0.95	5%	144°		12
50	Custom temperature probe		0	100%			01

B.   EXPERIMENTAL PROCEDURE

The Allison-Chalmers compressor was started and allowed to warm up. Once warm up was attained and operation was deemed normal, air was delivered to the TCR

support systems. These systems include the balance piston and the air driven oil mist system.

Once all support systems were running optimally the experiment could commence. Supply air was delivered to the drive turbines which drove the test compressor rotor to the desired corrected operating speed. The speed of the rotor required correcting based on the atmospheric conditions of the day, which were taken periodically during the experiment using a Taylor Sling Psychrometer, shown in Figure 15. The upstream electric throttle was initially in the full open position to allow 100 percent mass flow to the test compressor. To emulate an increase of back pressure the electric throttle was incrementally closed to restrict mass flow to the test compressor. The closures of the electric valve were moderate at the beginning of testing; however, as the test compressor approaches a stall condition the closures were made in the smallest possible increments achievable. The near stall conditions were recognized by real time plotting of the speed line. Data measurements were recorded at each incremental change to the electric throttle.

Figure 15. Taylor Sling Psychrometer

Additional parameters monitored during test were vibrations in the test compressor and drive turbine areas via accelerometers, axial strain on the shaft via strain gages located in front of the balance piston, and the corrected speed of the test compressor rotor. Vibrations were required to be below a particular threshold in order to maintain integrity if the test compressor and TCR components, as well as, the ability to ensure the best data measurements possible. Axial strain of the shaft changed during testing as speed changes to the rotor were incurred, also when the mass flow was reduced. The corrected speed of the rotor would also change when the mass flow was reduced. Each parameter was constantly monitored to ensure the equipment was operating in a safe condition and the measurements taken would produce the best results.

C.   DATA ACQUISITION AND REDUCTION

The Hewlett-Packard Visual Engineering Environment (HPVEE) data acquisition program developed by Gannon [7] was the same used in previous studies conducted by Drayton [4] and Lehrfeld [5]. This program measured the steady state pressures and temperatures and was summarized by Drayton [4]. The temperatures and pressures were mass-averaged to calculate the test compressor performance.

THIS PAGE INTENTIONALLY LEFT BLANK.

III. TASR/TS STAGE

This chapter shows the experimental results of Drayton's [4] designed TASR paired with Lehrfeld's designed TS. The purpose for inclusion of this chapter is Lehrfeld's design was not experimentally tested during his study. His design has been tested and the results and comparison are given.

A. EXPERIMENTAL RESULTS

Experimental testing was conducted in the rotor only and TASR/TS stage configuration. The TS was set to 6 different clocked positions during the experimental testing phase of this study. All experimental testing was done with a 0.508 mm (0.02 in) tip gap. Tables 2 and 3 list the operational speeds and the configurations tested. Figures 16 and 17 show the experimental results of the pressure ratio and efficiency.

Table 2.   List of Operational Speeds Tested.

Operational Speed percent	60	70	80	90	95	100
Revolutions Per Second	16,200	18,900	21,600	24,300	25,650	27,000

Table 3.   List of Test Compressor Configurations Tested.

Test Compressor Configuration	Rotor only	-20	-10	0 (BL)	+10	+30	+50
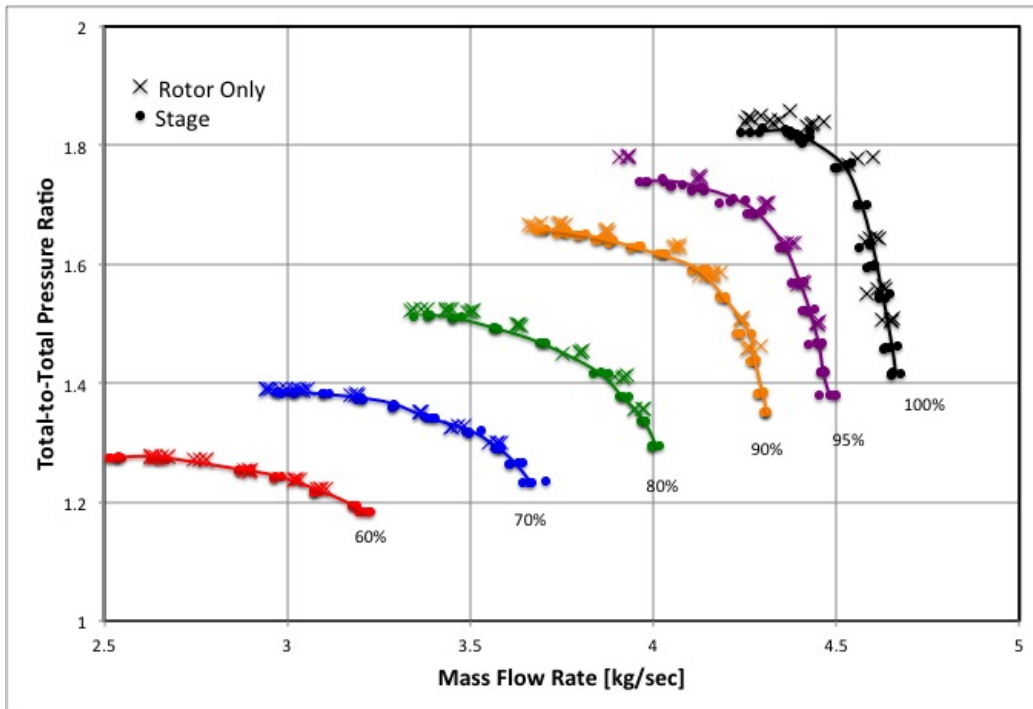
Figure 16. Pressure Ratio at Various Operating Speeds at the Baseline Stage Setting and Rotor-Only Configuration.
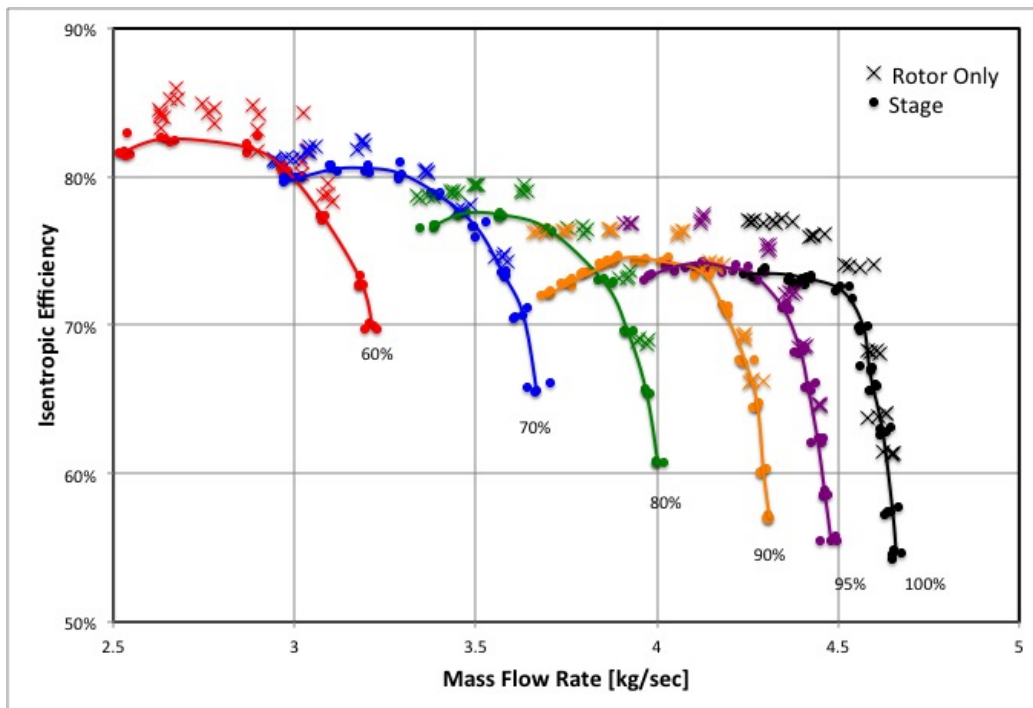
Figure 17. Isentropic Efficiency at Various Operating Speeds at the Baseline Stage Setting and Rotor-Only Configuration.

Table 4 summarizes the experimental results from all tested configurations at 100 percent operational speed.

Table 4.   Performance Results at 100 Percent Operational Speed.

	Peak PR[-]	Peak Efficiency%	Mass Flow Range
Rotor-Only	1.86	77.2	8.67
-20	1.82	71.6	7.16
-10	1.85	74.6	10.48
BL	1.83	73.8	9.30
+10	1.84	73.3	7.98
+30	1.83	72.6	8.61
+50	1.82	72.2	8.39

The results were non-dimensionalized to show stage loading and efficiency versus flow coefficient at all the operational speeds tested. Stage loading (Φ), equation 1, is a ratio between the axial speed of the air and the blade tip speed. The axial speed (C_Z), equation 2, is a ratio between the mass flow rate and a product of the density and the cross-sectional area of the flow. Flow coefficient (ψ), equation 3, is a ratio between the change of enthalpy (H) and the tip speed of the rotor squared. The change of enthalpy, equation 4, is equated to the product of the specific heat capacity at constant pressure and the change of temperature between outlet (T_{03}) and inlet (T_{01}) of the test compressor.

$$\Phi = \frac{C_Z}{U} \tag{1}$$

with

$$C_z = \frac{\dot{m}}{\rho \cdot A} \tag{2}$$

$$\Psi = \frac{\Delta H_\circ}{U^2} \tag{3}$$

with

$$\Delta H_\circ = c_P \cdot \left(T_{03} - T_{01} \right) \tag{4}$$

Figures 18 through 20 are the stage loading versus flow coefficient plots for 60 percent, 80 percent, and 100 percent operational speeds tested. Figures 21 through 23 are the efficiencies versus flow coefficient plots for 60 percent, 80 percent, and 100 percent operational speeds tested.
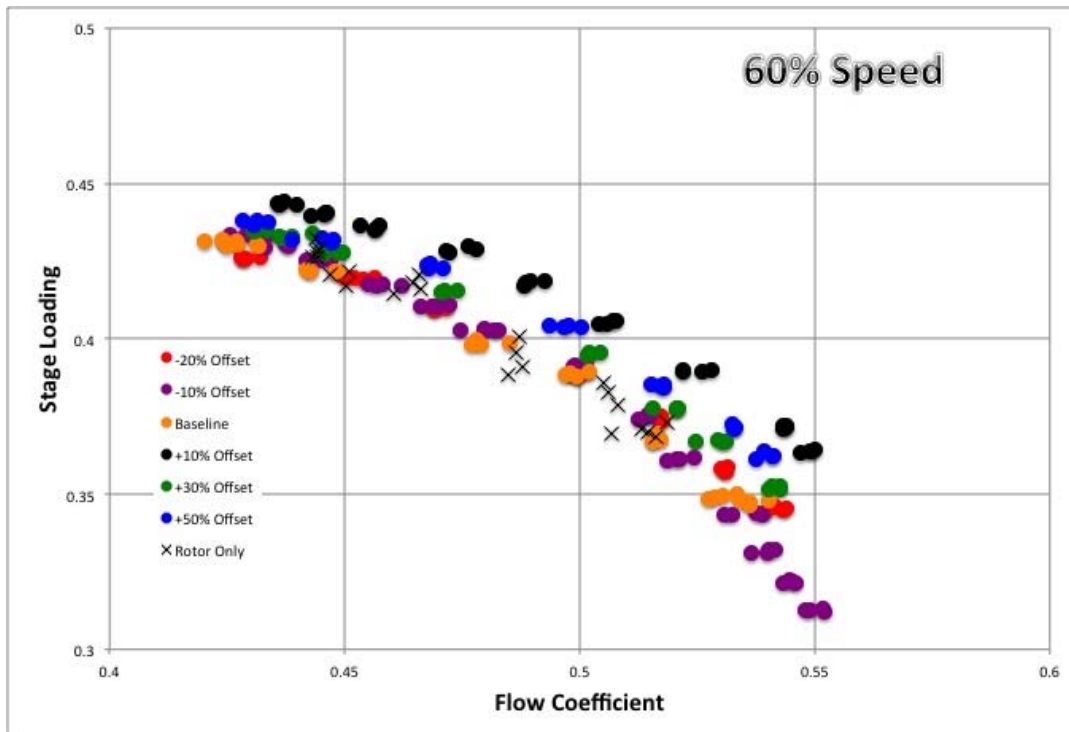
Figure 18. Stage Loading at 60 Percent Speed.
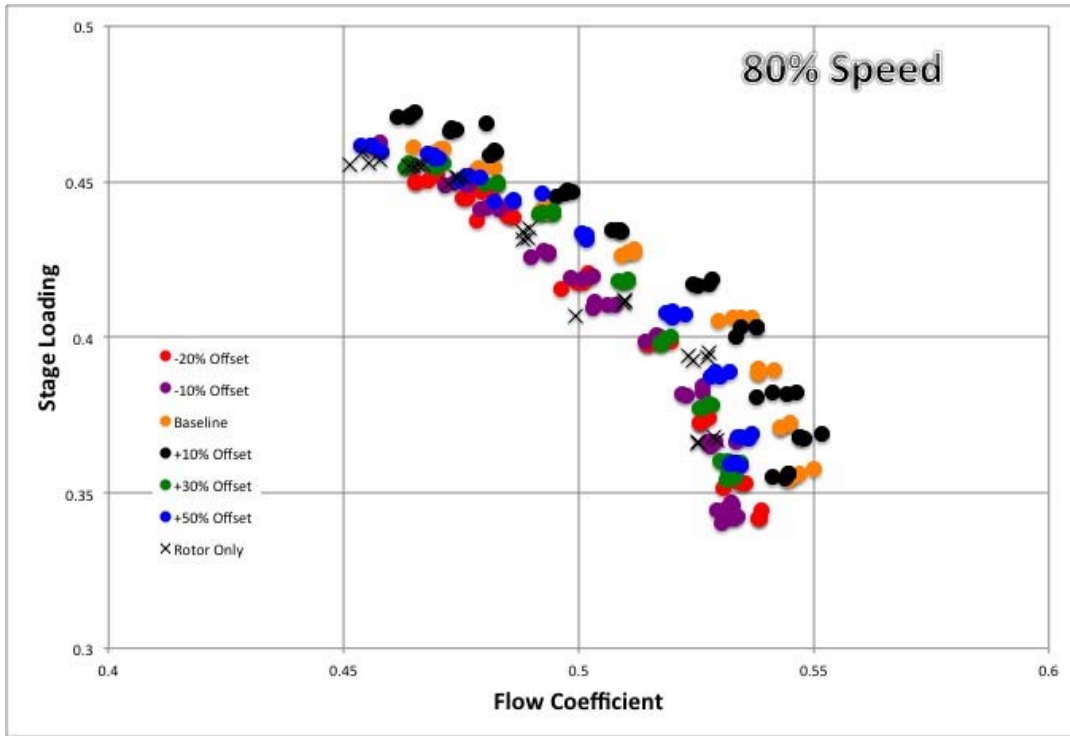
Figure 19. Stage Loading at 80 Percent Speed.
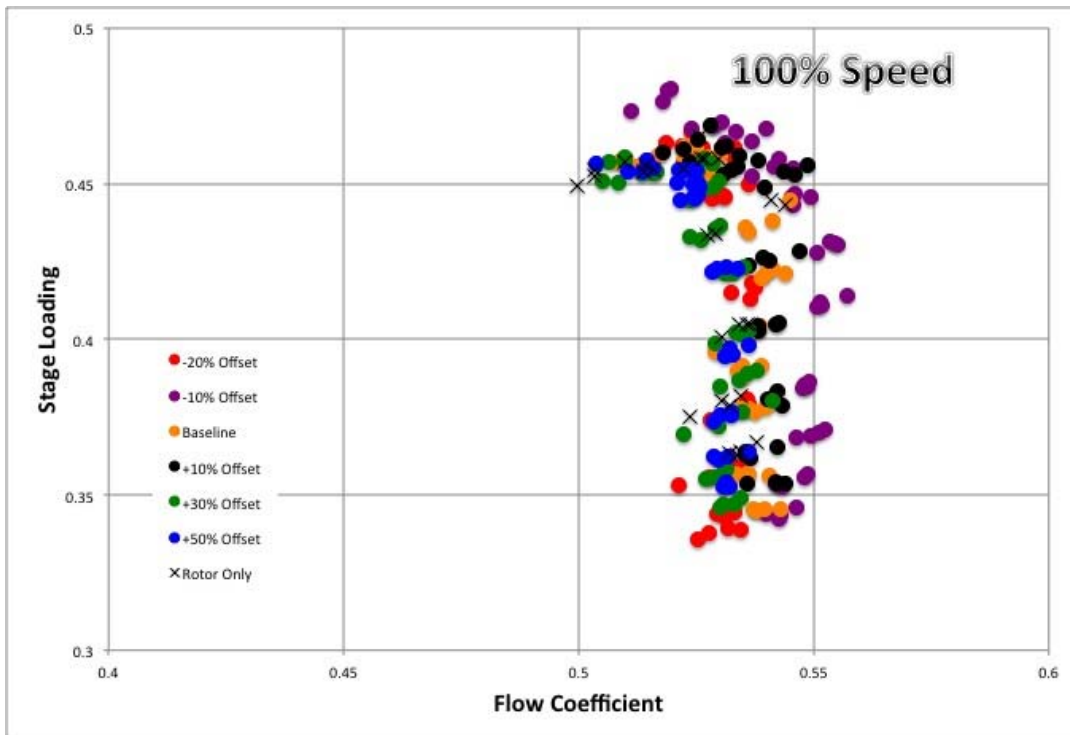
Figure 20. Stage Loading at 100 Percent Speed.

29
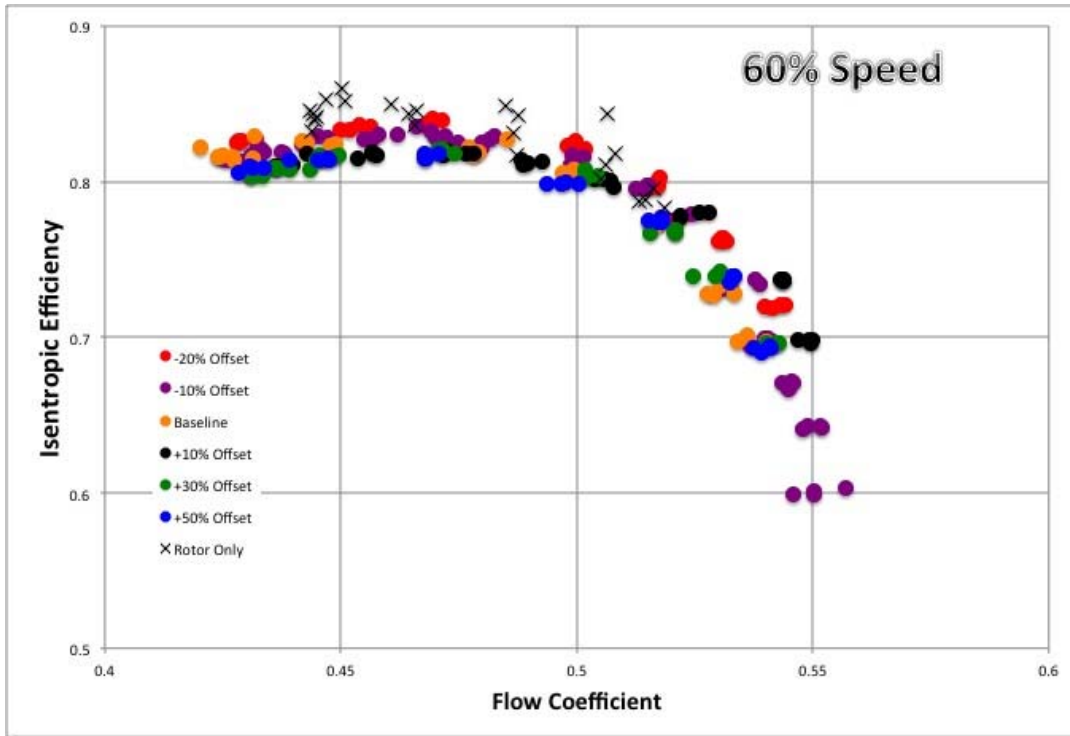
Figure 21. Isentropic Efficiency at 60 Percent Speed.
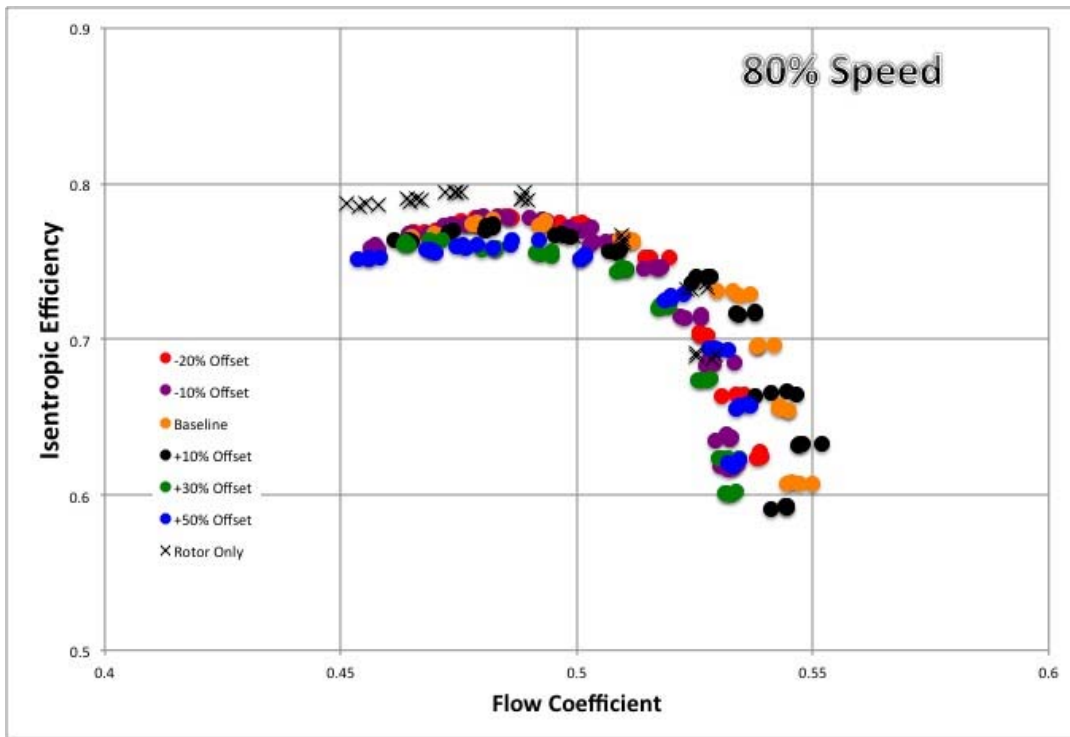
Figure 22. Isentropic Efficiency at 80 Percent Speed.
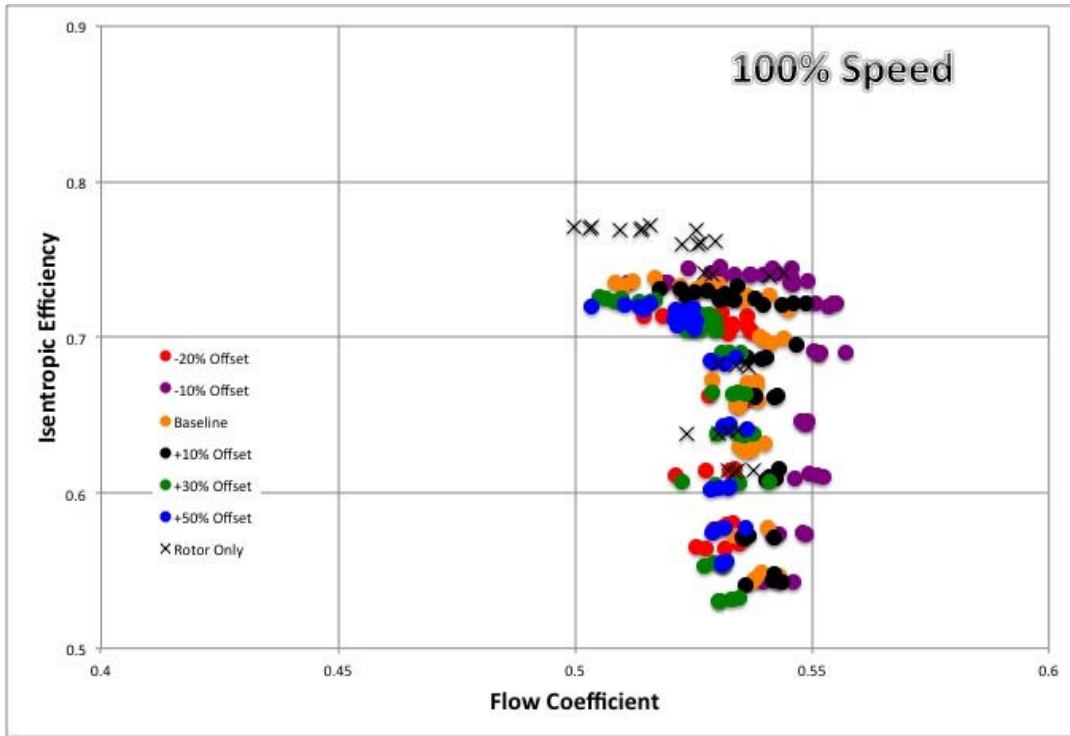
Figure 23. Isentropic Efficiency at 100 Percent Speed.

B.   COMPARISON

Table 5 shows the results from Drayton's [4] and Lehrfeld's [5] work; as well and the results from this study. Drayton incorporated multiple TGs in his study, which are included here for comparison value.

Table 5.   TASR and Stage Numerical and Experimental Comparison at 100 Percent Operational Speed.

	tip gap mm(in)	Peak PR [-]	Peak Efficiency [%]	Mass Range [%]
Num TASR	0.25 (0.010)	1.92	80	6.0
Exp TASR	0.91 (0.036)	1.69	72	7.5
Exp TASR	0.51 (0.020)	1.86	77.2	8.7
Num BL	0	1.97	77.5	8.4
Exp BL	.51 (0.020)	1.83	73.8	9.3
Exp +10	.51 (0.020)	1.84	73.3	8.0
Exp +30	.51 (0.020)	1.83	72.6	8.6
Exp +50	.51 (0.020)	1.82	72.2	8.4
Exp -10	.51 (0.020)	1.85	74.6	10.5
Exp -20	.51 (0.020)	1.82	71.6	7.2

Lehrfeld also evaluated the stage numerically with positive and negative offsets at 100 percent operational speed. These simulations did not incorporate a tip gap over the TASR blades. Figures 24 and 25 show the experimental results of pressure ratio and efficiency for positive offsets.
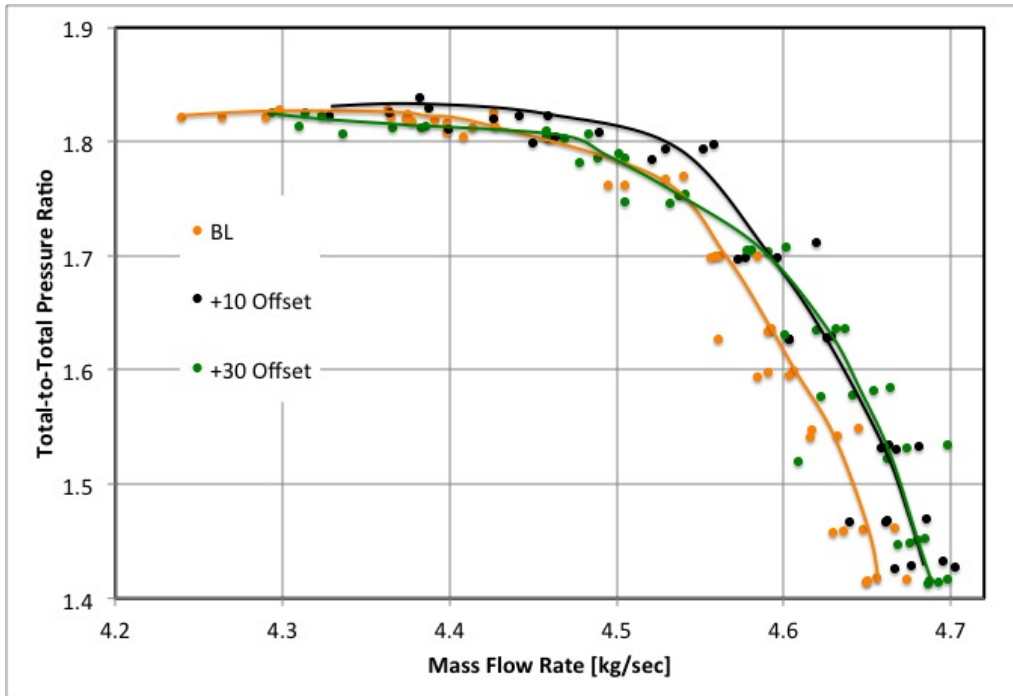
Figure 24. Experimental Positive Offset Pressure Ratio.
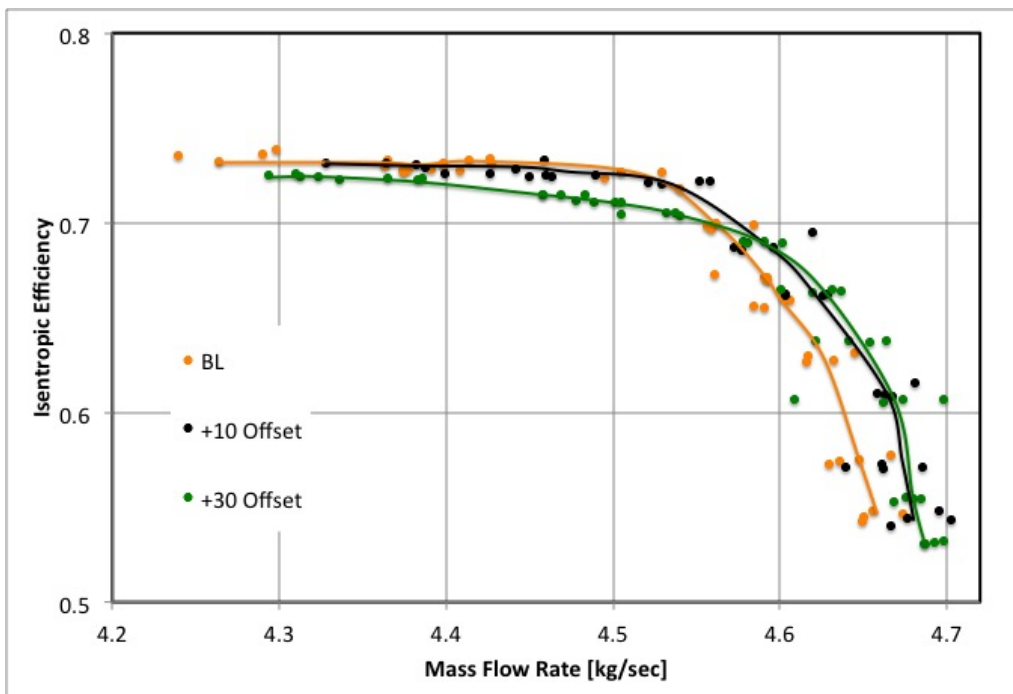
Figure 25. Experimental Positive Offset Efficiency.

33

Lehrfeld identifies the results for the numerically derived positive offsets exhibit an increased pressure ratio; however, they are not as well behaved as the baseline setting [5]. Furthermore, the efficiencies were lower than the baseline setting. Lehrfeld interprets these results as a fact that the baseline geometry was designed to be the most behaved setting. The experimental results for a positive offset setting do not exhibit the same peak pressure ratio effects. The +10 percent setting was the only setting with a greater peak pressure ratio value than the baseline setting. The efficiency map in Figure 25 displays different trends than Lehrfeld's predicted numerical results from his thesis. The peak efficiencies are as Lehrfeld predicted; however, the experimental baseline setting results show the compressor operates through a lower mass flow rate range. Also observed in Figure 25 the baseline setting undercuts the positive offsets then climbs to a higher peak efficiency.

Lehrfeld's numerically derived negative results show an inverse in the performance of the compressor. The pressure ratios were lower and the efficiencies were higher compared to the baseline setting. Figures 26 and 27 show the experimental results of pressure ratio and efficiency for negative offsets. The numerical predictions of a higher pressure ratio for the baseline setting only holds true against the -20 percent setting. The -10 percent setting exceeds the baseline peak pressure ratio. The same is observed for the efficiencies. The -10 setting exceeds the baseline setting where the -20 setting falls below the baseline setting; this observation counters the predicted performance from Lehrfeld's work. The most notable observation when comparing the pressure ratio and efficiency performance maps is the mass flow range. The experimental results show the compressor operates at a higher mass flow rate than predicted.
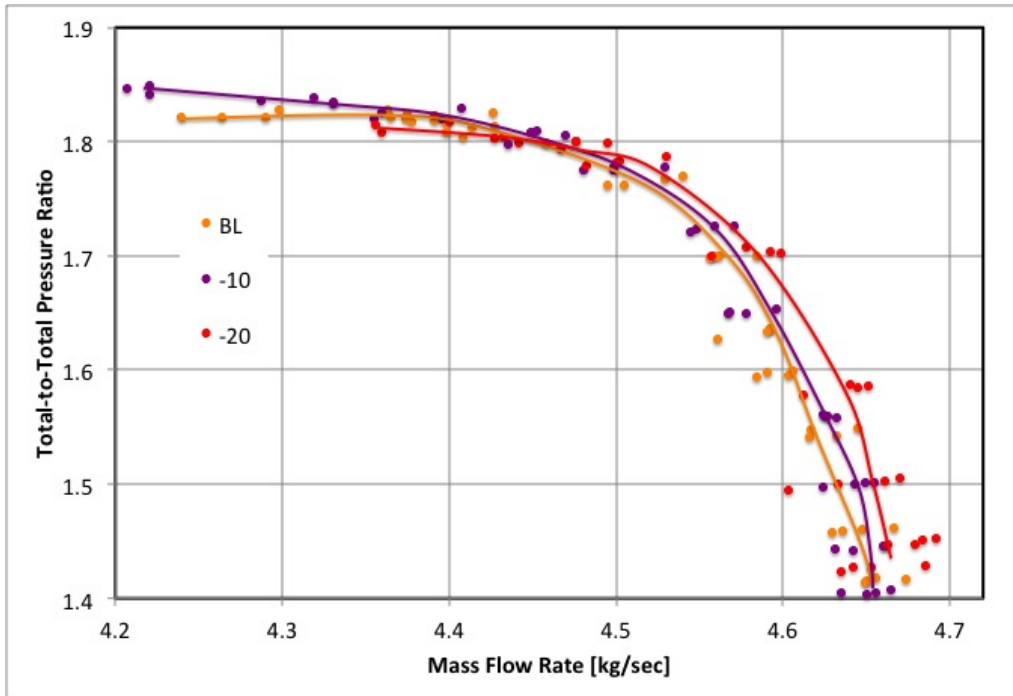
Figure 26. Experimental Negative Offset Pressure Ratio.
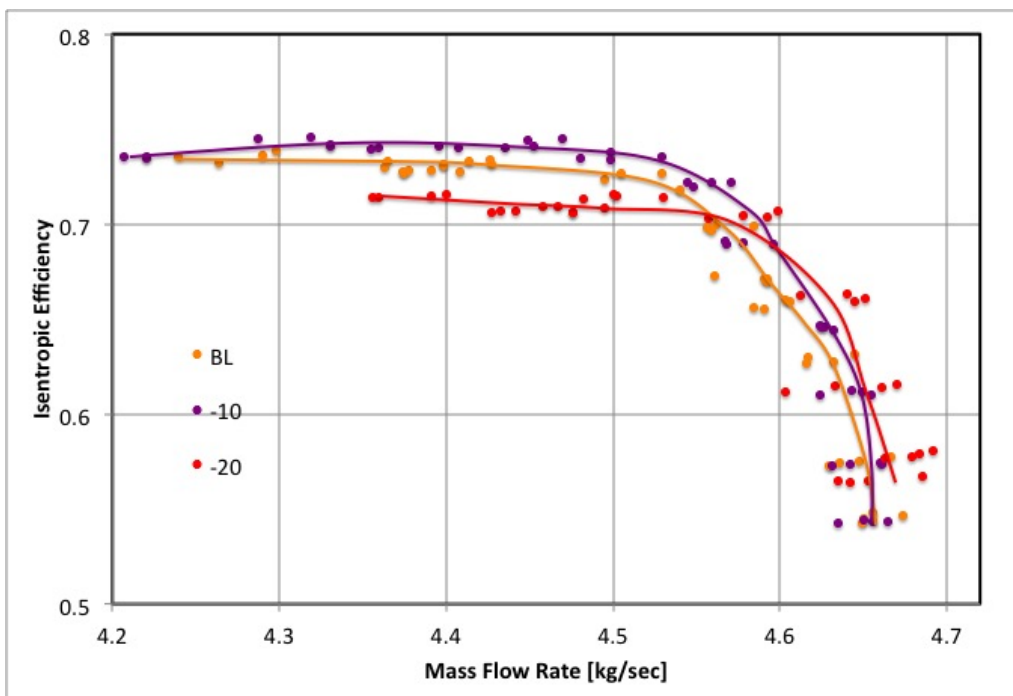
Figure 27. Experimental Negative Offset Efficiency.

35

THIS PAGE INTENTIONALLY LEFT BLANK.

IV.   TASR HOT AND COLD SHAPE ANALYSIS

The design process developed by Drayton [4] was missing a key implementation for comparison to the design goals. The comparisons Drayton made were based on the CFX simulations conducted on the cold shape of the rotor blades. These simulations did not take into account the deformations that existed in the rotor once a rotational velocity and gas loading was enacted on it experimentally. In practice these forces were present on the rotor when spinning and it took on a new deformed geometry that experimental results were derived from. The new geometry that was formed was termed the hot shape of the rotor as is common in the turbomachinery community. Figure 28 shows the rotor blades deformation.
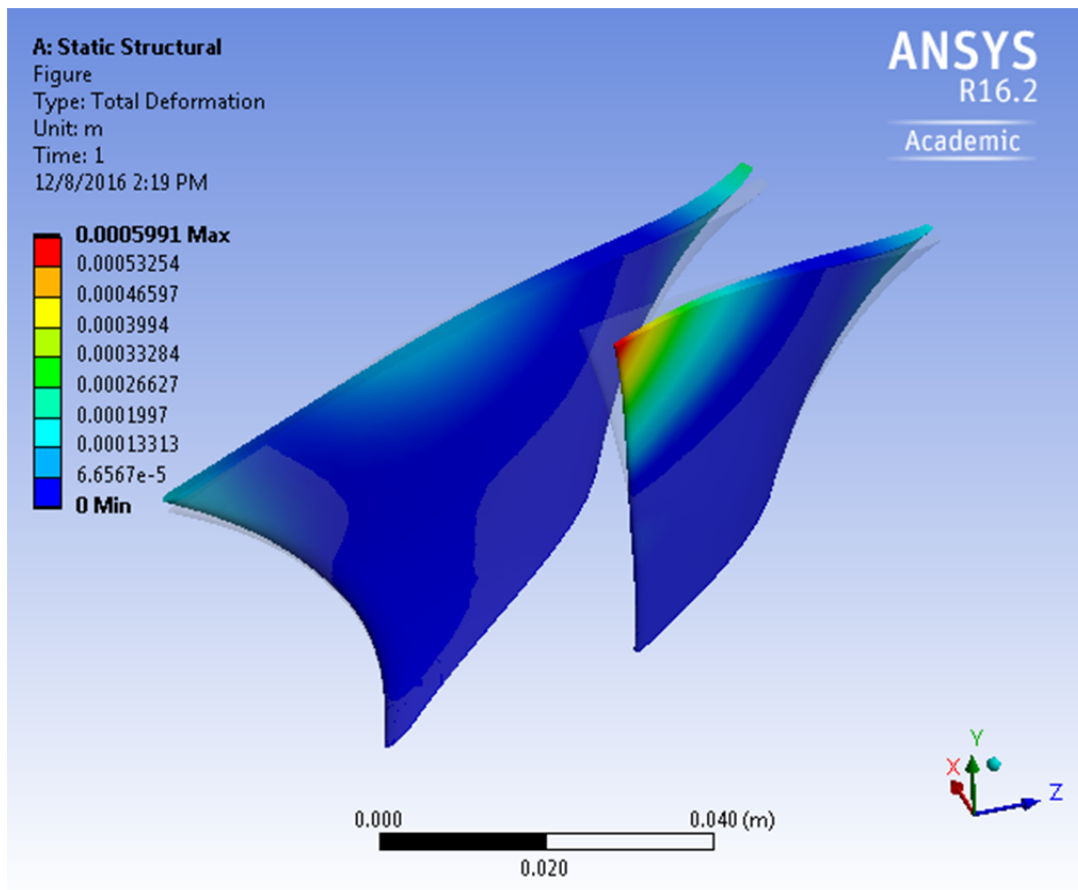
Figure 28. Rotor Blades Deformation with Rotational Velocity and No Gas Loading.

37

Figure 28 depicts the deformation the rotor blades experienced with only an 18,900 RPM velocity and no gas loading present on the blades. They exhibited approximately a 0.6 mm (0.024 in) total mesh displacement. Figure 29 depicts the deformation the blades experienced under the same rotational velocity as well as gas loading and they exhibited approximately a 0.85 mm (0.033 in) total mesh displacement.
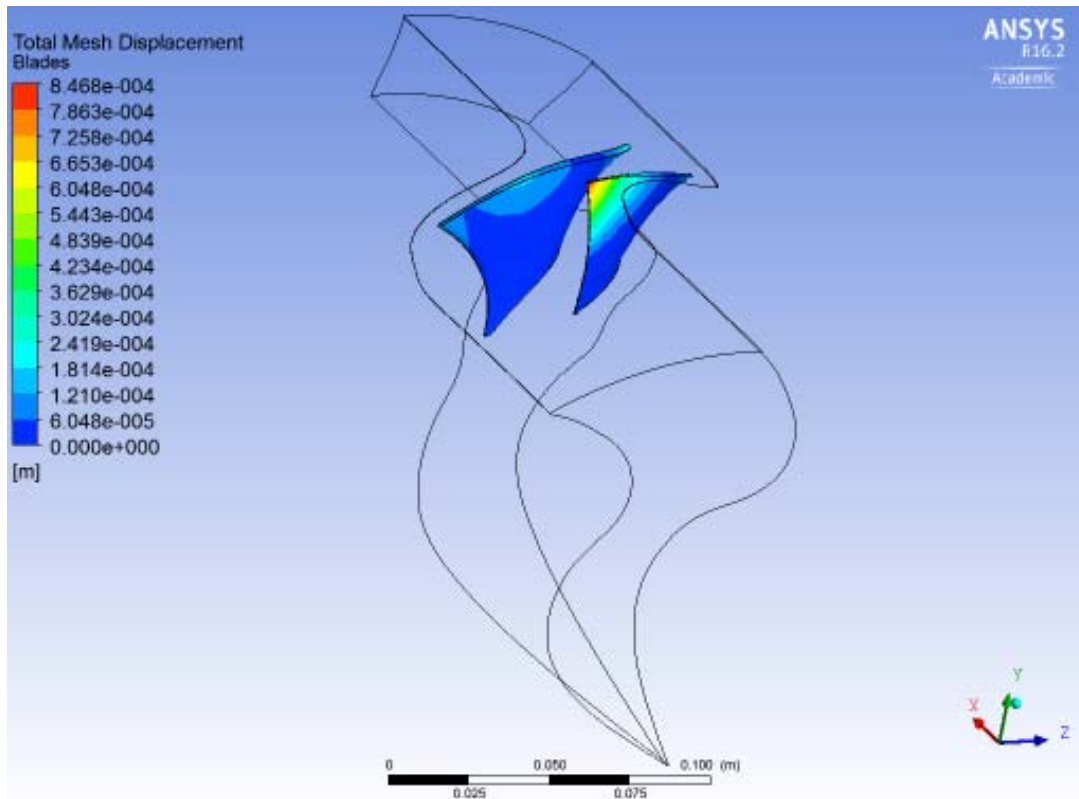
Figure 29. Rotor Blades Deformation with Rotational Velocity and Gas Loading.

Figure 30 shows the gas mesh deformation at mid-span of the blades. Figure 31 shows the gas mesh deformation at near tip of the blades. It was observed the near tip gas mesh deformation measured approximately the same as the total blade mesh deformation. Figures 28 through 31 emphasize the hot shape geometry change and incorporating the hot shape of the rotor to derive numerical performance maps that could be compared to design goals will produce an improvement to Drayton's design procedure.
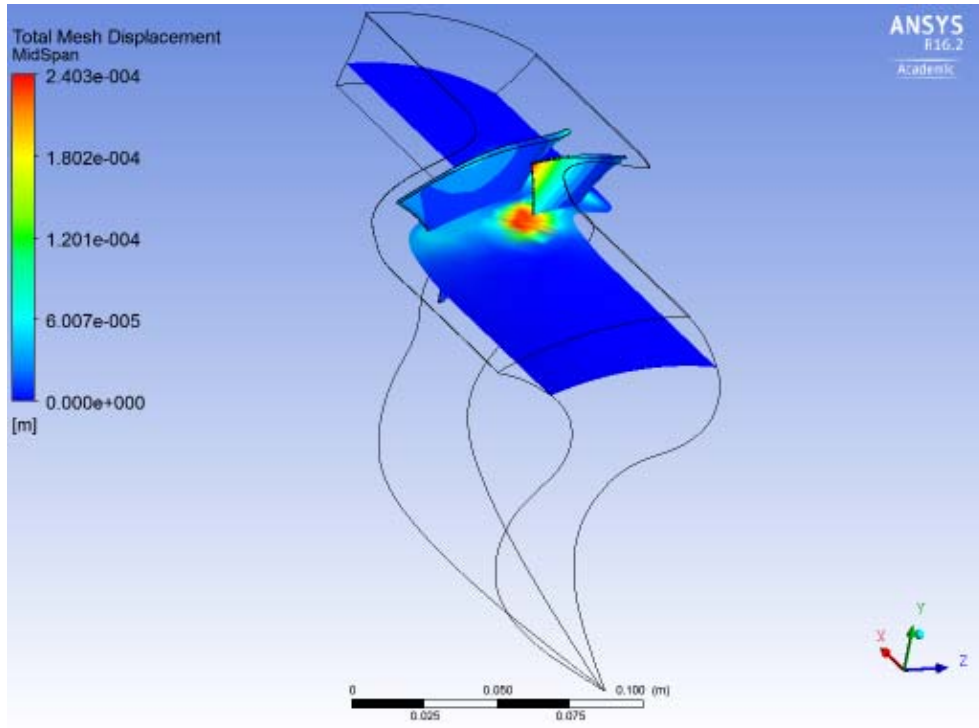
Figure 30. Gas Mesh Deformation at Mid-Span of the Blades
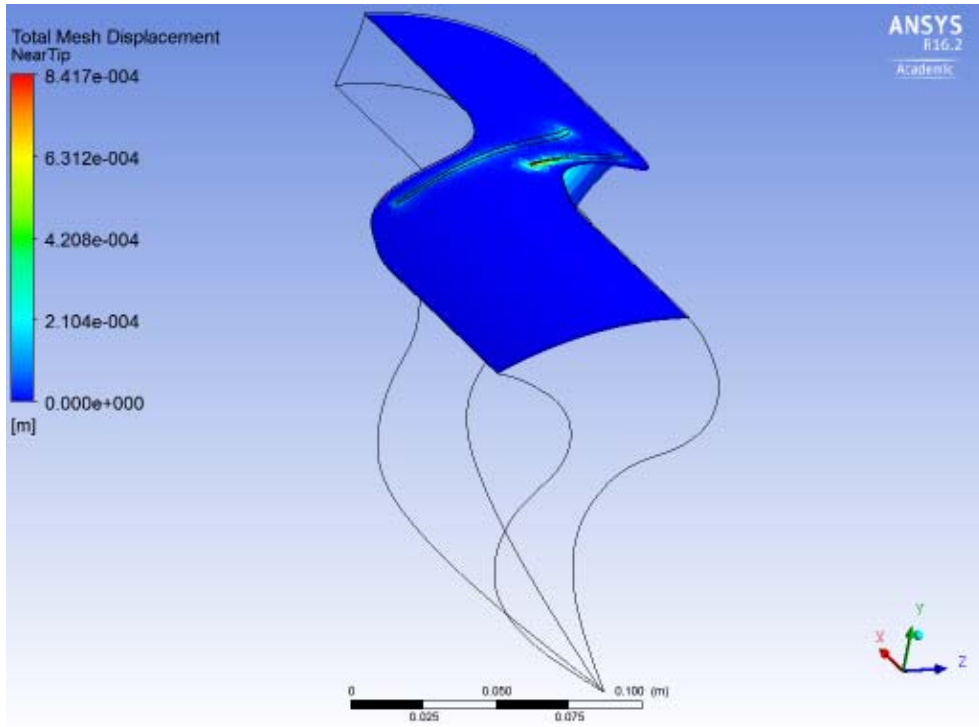
Figure 31. Gas Mesh Deformation at Near Tip of the Blades

This section of study focused on the 70 percent speed of the rotor. This was due to fatal simulation testing at higher speeds. The mesh deformation in the gas was too large for the mesh elements to handle. This caused negative element volumes, which terminates the test run and files no solution data.

A.   TASR HOT SHAPE

The hot shape of any rotor is made up of two components. The first is the rotational velocity of the rotor and the second is the gas loading the rotor undergoes. The rotational velocity component of the deformation accounts for the largest percentage of deformation. This study utilized a two-way fluid-structure interaction (FSI) between the structural blades of the rotor and gas surrounding the blades that cause a load on the blades. The project schematic setup utilized the static structural (SS) and the CFX analysis systems to run the simulation. Figure 32 shows the project schematic setup.
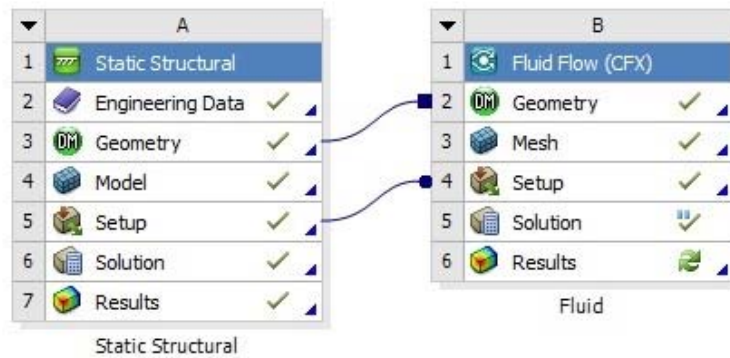
Figure 32. Project Schematic Setup for FSI

Instructions for setting up a two-way FSI are given in Appendix C. Figure 33 shows the two-way FSI solution procedure used for this study.
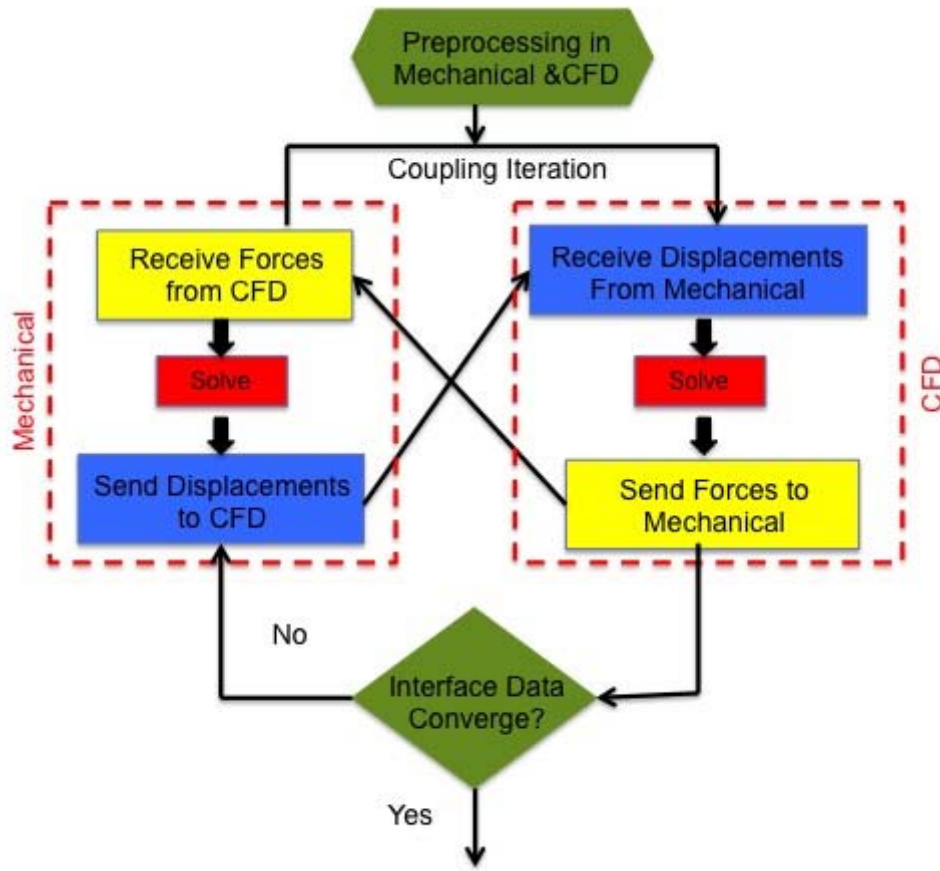
Figure 33. Two-Way FSI Solution Procedure.

The solution procedure began in the SS where the displacements of the rotor blades were solved. Those displacements were sent to CFD. CFD began solving for the reaction forces in the gas from the displacements of the rotor blades. Those forces were sent to SS where the displacements were again solved. The back and forth between the two coupled systems was the coupling iteration. Which could be set to a user specified quantity or a specific convergence identified to complete the solution. The procedure for capturing the hot shape of a rotor can be incorporated into TPL's rotor design process by setting up the project schematic in the ANSYS working directory. However, the specific setup required for the FSI would have to be investigated.

41

B.   NUMERICAL SIMULATION

The geometries used were derived from those generated by Drayton [4] during his study with some modifications. All previous numerical testing was done with the cold shape where only the gas path was utilized and the area in the gas path where the blades would be were set as a wall boundary condition. Implementing the hot shape required a generation of the solid blades. This was done using the gas path as a template. Using SW, surface fills were inserted into the hub and casing where the ends of the blades would fit. Figure 34 shows the gas path template used with surface fills at the top and bottom of the blades as well as annotations for the purpose of orientation.
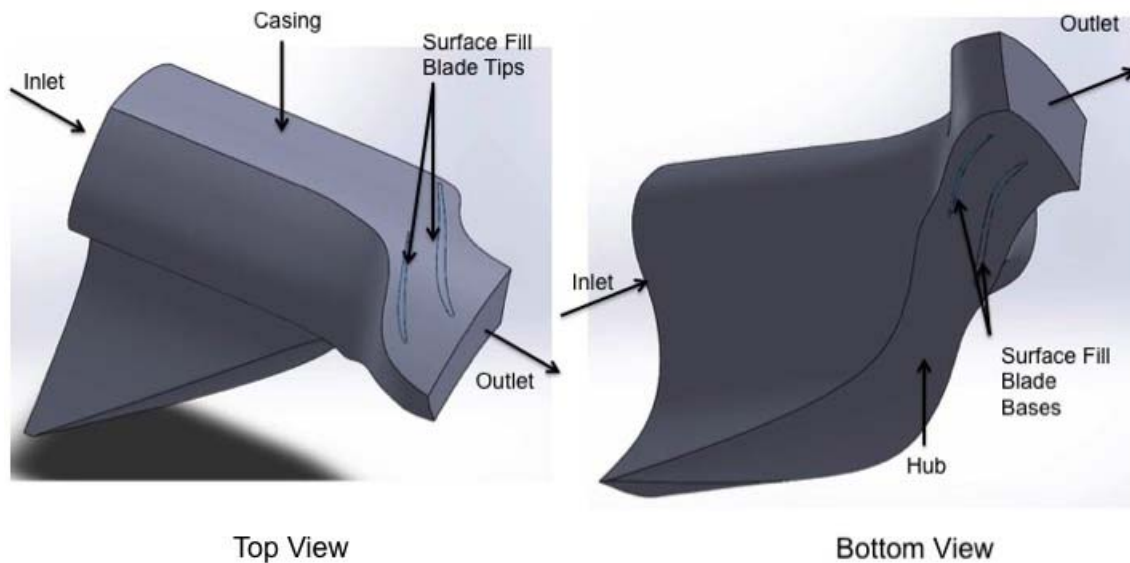
Figure 34. Gas Path Template with Surface Fills.

Once the surface fills were placed they were used as a source and target and the face inside the gas path template was used as guide to create two knitted parts, the main blade and the splitter blade. Alterations to the gas path were made to incorporate a .508 mm (0.02 in) tip gap; also the outlet region of the gas path was required to be extended to ensure shocks would not travel passed the outlet boundary condition domain.

Table 6 shows the testing parameters used to compare the hot shape of a rotor to the cold shape of a rotor. The ideal (standard) atmospheric conditions were 288.15 K for temperature and 101,300 Pa for pressure. The hot shape using a shear stress transport (SST)—gamma theta turbulence model utilized the measured gas properties taken during experimental testing in order to match those properties for better numerically derived results.

Table 6.   Numerical Testing Parameters.

Simulation	Turbulence/ Transition	Gas Properties	Rotational Velocity
Cold Shape	k-epsilon—N/A	Ideal (standard)	18,900 RPM
Hot Shape	k-epsilon—N/A	Ideal (standard)	18,900 RPM
Hot Shape	SST—gamma theta	Ideal (matched)	18,900 RPM

C.   RESULTS

Numerical simulations were conducted and the results are included here. A CFX mesh and physics report is included in Appendix D and E for the k-epsilon turbulence model cold and hot shape simulation, respectively. Figures 35 and 36 show rotor-only numerically derived and experimental results of pressure ratio and isentropic efficiency. The hot and cold shape simulations using the k-epsilon turbulence model had the same boundary conditions and gas properties. Furthermore, each alteration to the backpressure was changed by the same incremental amount. The hot and cold shape simulations showed the same trends in their speed line paths. However, the hot shape simulation shows an extension in mass flow range. An attempt was made to better match the experimental results. The turbulence model was changed to a SST—gamma theta model and the gas properties were matched to emulate the same pressures and temperatures measured during testing. The results showed a shift in the speed line toward the experimental results for that simulation.
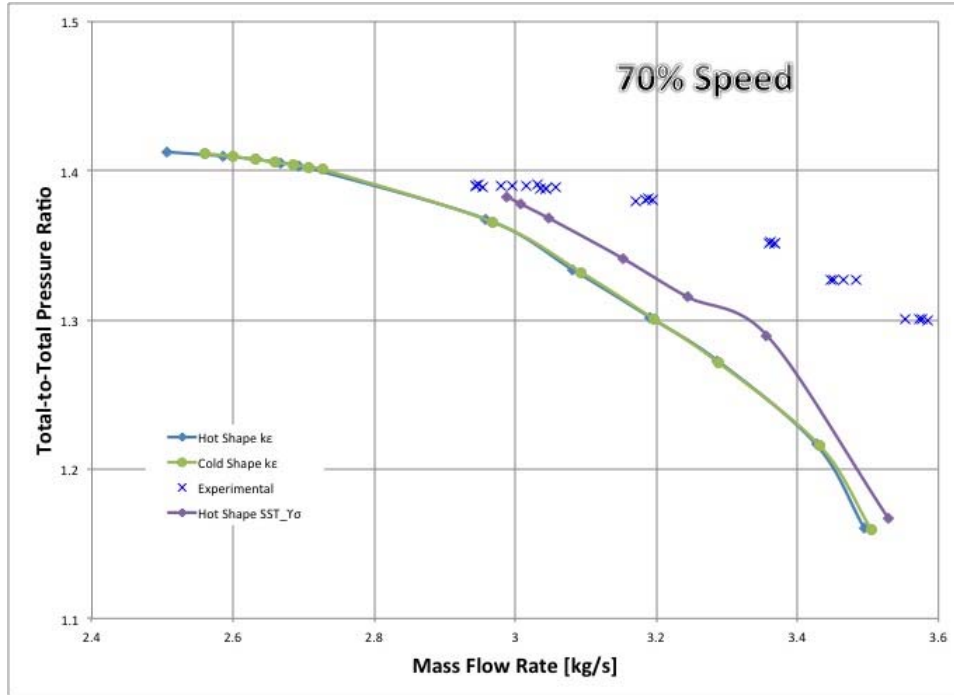
Figure 35. Pressure Ratio at 70 Percent Operating Speed at the Rotor-Only Configuration.
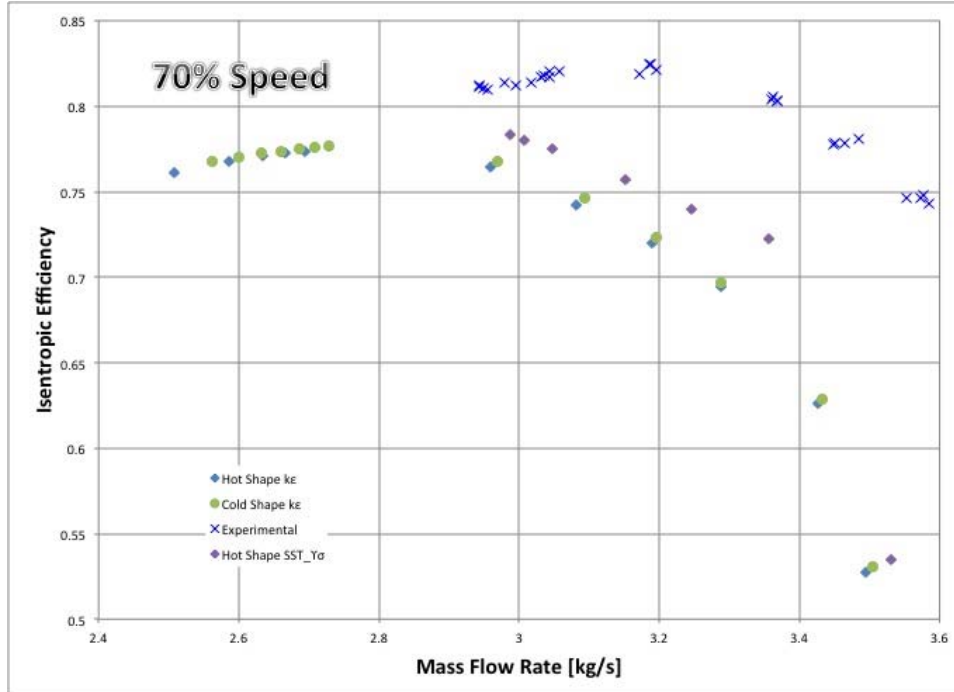
Figure 36. Isentropic Efficiency at 70 Percent Operating Speed at the Rotor-Only Configuration.

V.   CONCLUSIONS AND RECOMMENDATIONS

A.   CONCLUSIONS

The objectives of this study were to experimentally determine the performance of the TASR/TS stage at various stator clocking positions, as well as, develop a procedure to capture the hot shape of a rotor and incorporate the hot shape into the TPL's design process. The secondary objective was to observe the effect of two different turbulence models in the prediction of rotor-only performance.

The numerically determined optimum circumferential relationship between the stator leading blade and trailing was designed as the baseline setting of the TS. Experimental results observed from this study show otherwise. At 100 percent design speed the TS setting that exhibited the best performance in both stage loading and isentropic efficiency was the negative 10 percent setting. At lower speeds, the optimum setting for stage loading was observed to be the positive 10 percent setting and for isentropic efficiency the negative 20 percent setting was the optimum setting. The overall design of the TS was proved to be a great performer. This fact was observed from the baseline setting pressure ratio versus mass flow rate performance maps compared to the rotor-only performance there was little disparity between the results.

The procedure to capture the hot shape of a blade using a numerical simulation was identified. The manner in which it was established enabled it to be easily incorporated into the TPL's design process. The project schematic setup should be placed in the working project for the design process. One area of concern for incorporating the hot shape into the design process was the specific setup for the FSI within the analysis systems. Further investigation will be required to ensure interfaces are active between the iterations of the design geometry. The comparison of the hot shape to cold shape showed the hot shape caused a larger mass flow range.

Two turbulence models were used to predict the performance of the rotor-only configuration. These were the k-epsilon and the SST turbulence models. The gamma theta transition model was used in conjunction with the SST turbulence model The results

showed the SST—gamma theta model mapped performance closer to the experimental results.

B.   RECOMMENDATIONS

The hot shape procedure could only be tested at 70 percent speed. This was due to negative volume elements error that occurred during simulation. These errors arose after incorporating the tip gap. The elements in the region of the TGs would stretch and become thin as the blades deformed. A method was not identified to form a structured mesh in the tip gap regions to sustain the element thinning. Recommend generating tip gap regions separately from the rest of the gas path. The tip gap generation should involve multiple layers of sweepable bodies. This method could cause a manual means to constructing a structured mesh in the tip gap regions. Once such a structured mesh is implemented a higher speed yield for simulations should be attainable.

Recommend a continued investigation into the SST—gamma theta model. The y+ values in these results were not low enough to promote the best predictions in performance.

APPENDIX A. REPETIER 3-D PRINTER SOFTWARE CONFIGURATION

The following is the printer configuration for the set tool molds generated.

```
# generated by Slic3r 1.2.9 on Tue Nov 22 11:37:12 2016
avoid_crossing_perimeters = 0
bed_shape = 0x0,400x0,400x400,0x400
bed_temperature = 75
before_layer_gcode =
bottom_solid_layers = 3
bridge_acceleration = 0
bridge_fan_speed = 100
bridge_flow_ratio = 1
bridge_speed = 60
brim_width = 10
complete_objects = 1
cooling = 1
default_acceleration = 0
disable_fan_first_layers = 1
dont_support_bridges = 0
duplicate_distance = 6
end_gcode = ;(end of the file, cooldown routines)\nM104 S0 T0;
(Turn off extruder temperature Toolhead 0)\nM104 S0 T1;
(Turn off extruder temperature Toolhead 1)(Support)\nM140 S0 T0;
(set heated-build-platform temperature)\nG91;
\nG28 X0 Y0;
\nG1 Y400 F5000;
\nM84 (steppers off)\n(end of end.txt)
external_fill_pattern = concentric
external_perimeter_extrusion_width = 0
external_perimeter_speed = 70%
external_perimeters_first = 0
extra_perimeters = 1
extruder_clearance_height = 80
extruder_clearance_radius = 80
extruder_offset = 0x0
extrusion_axis = E
extrusion_multiplier = 1
extrusion_width = 0
fan_always_on = 0
fan_below_layer_time = 60
filament_colour = #FFFFFF
filament_diameter = 1.75
fill_angle = 45
fill_density = 30%
fill_pattern = 3dhoneycomb
first_layer_acceleration = 0
first_layer_bed_temperature = 65
```

```
first_layer_extrusion_width = 0
first_layer_height = 0.35
first_layer_speed = 30
first_layer_temperature = 200
gap_fill_speed = 20
gcode_arcs = 0
gcode_comments = 0
gcode_flavor = reprap
infill_acceleration = 0
infill_every_layers = 1
infill_extruder = 1
infill_extrusion_width = 0
infill_first = 1
infill_only_where_needed = 0
infill_overlap = 15%
infill_speed = 60
interface_shells = 0
layer_gcode =
layer_height = 0.3
max_fan_speed = 100
max_print_speed = 80
max_volumetric_speed = 0
min_fan_speed = 35
min_print_speed = 10
min_skirt_length = 0
notes =
nozzle_diameter = 0.5
octoprint_apikey =
octoprint_host =
only_retract_when_crossing_perimeters = 1
ooze_prevention = 0
output_filename_format = [input_filename_base].gcode
overhangs = 1
perimeter_acceleration = 0
perimeter_extruder = 1
perimeter_extrusion_width = 0
perimeter_speed = 30
perimeters = 3
post_process =
pressure_advance = 0
raft_layers = 0
resolution = 0
retract_before_travel = 2
retract_layer_change = 1
retract_length = 0
retract_length_toolchange = 10
retract_lift = 1
retract_restart_extra = 0
retract_restart_extra_toolchange = 0
retract_speed = 60
```

```
seam_position = random
skirt_distance = 25.9
skirt_height = 1
skirts = 2
slowdown_below_layer_time = 30
small_perimeter_speed = 30
solid_infill_below_area = 40
solid_infill_every_layers = 0
solid_infill_extruder = 1
solid_infill_extrusion_width = 0
solid_infill_speed = 60
spiral_vase = 0
standby_temperature_delta = -5
start_gcode = ; (beginning of start.txt)\nG90;
(Absolute Positioning)\nG28;
(Homing back to X, Y and Z zero endstops.)\nG92 X0 Y0 Z0;
(set origin to current position)\nG91;
(Set to Relative Positioning)\nG28;
(Homing back to X, Y and Z zero endstops.)\nG90;
(Set to Absolute Positioning ) \nG92 E0;
(zero the extruded length)\n;
(end of start.txt)
support_material = 0
support_material_angle = 0
support_material_contact_distance = 0.2
support_material_enforce_layers = 0
support_material_extruder = 1
support_material_extrusion_width = 0
support_material_interface_extruder = 1
support_material_interface_layers = 0
support_material_interface_spacing = 0
support_material_interface_speed = 100%
support_material_pattern = rectilinear-grid
support_material_spacing = 2.5
support_material_speed = 60
support_material_threshold = 0
temperature = 200
thin_walls = 1
threads = 3
toolchange_gcode =
top_infill_extrusion_width = 0
top_solid_infill_speed = 50
top_solid_layers = 3
travel_speed = 130
use_firmware_retraction = 0
use_relative_e_distances = 0
use_volumetric_e = 0
vibration_limit = 0
wipe = 0
xy_size_compensation = 0
```

THIS PAGE INTENTIONALLY LEFT BLAN
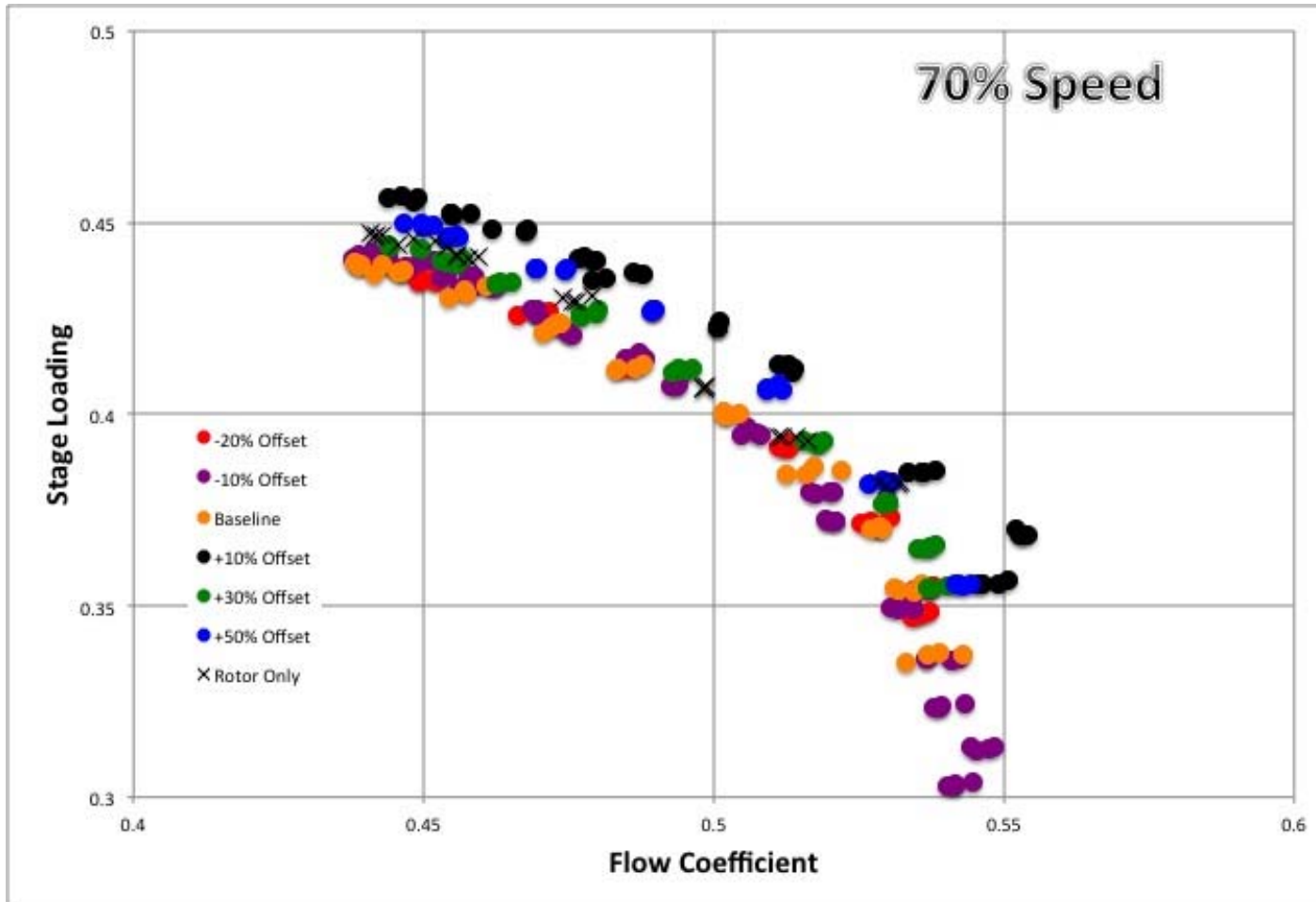
Figure 37. Stage Loading at 70 Percent Speed.

51
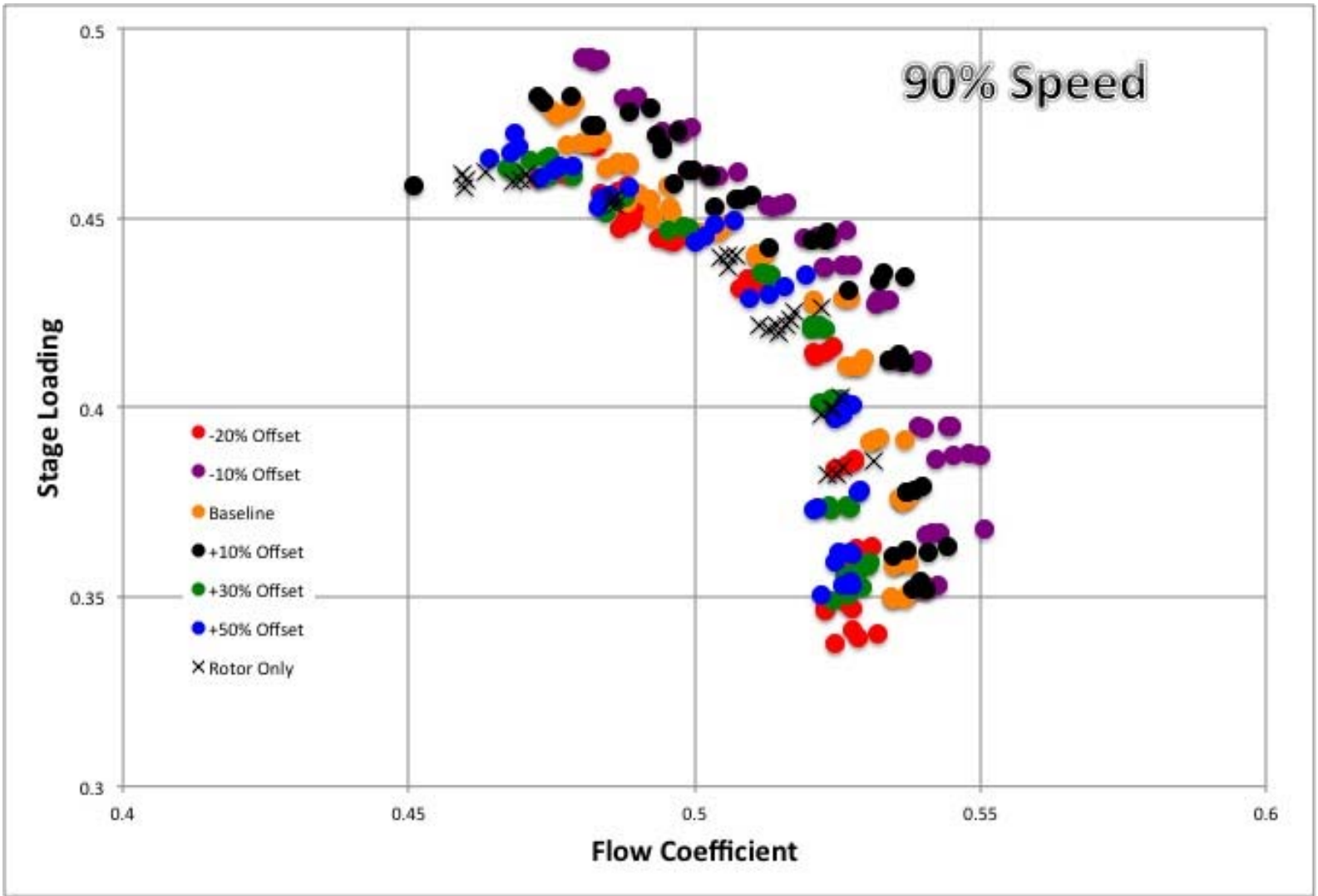
Figure 38. Stage Loading at 90 Percent Speed.
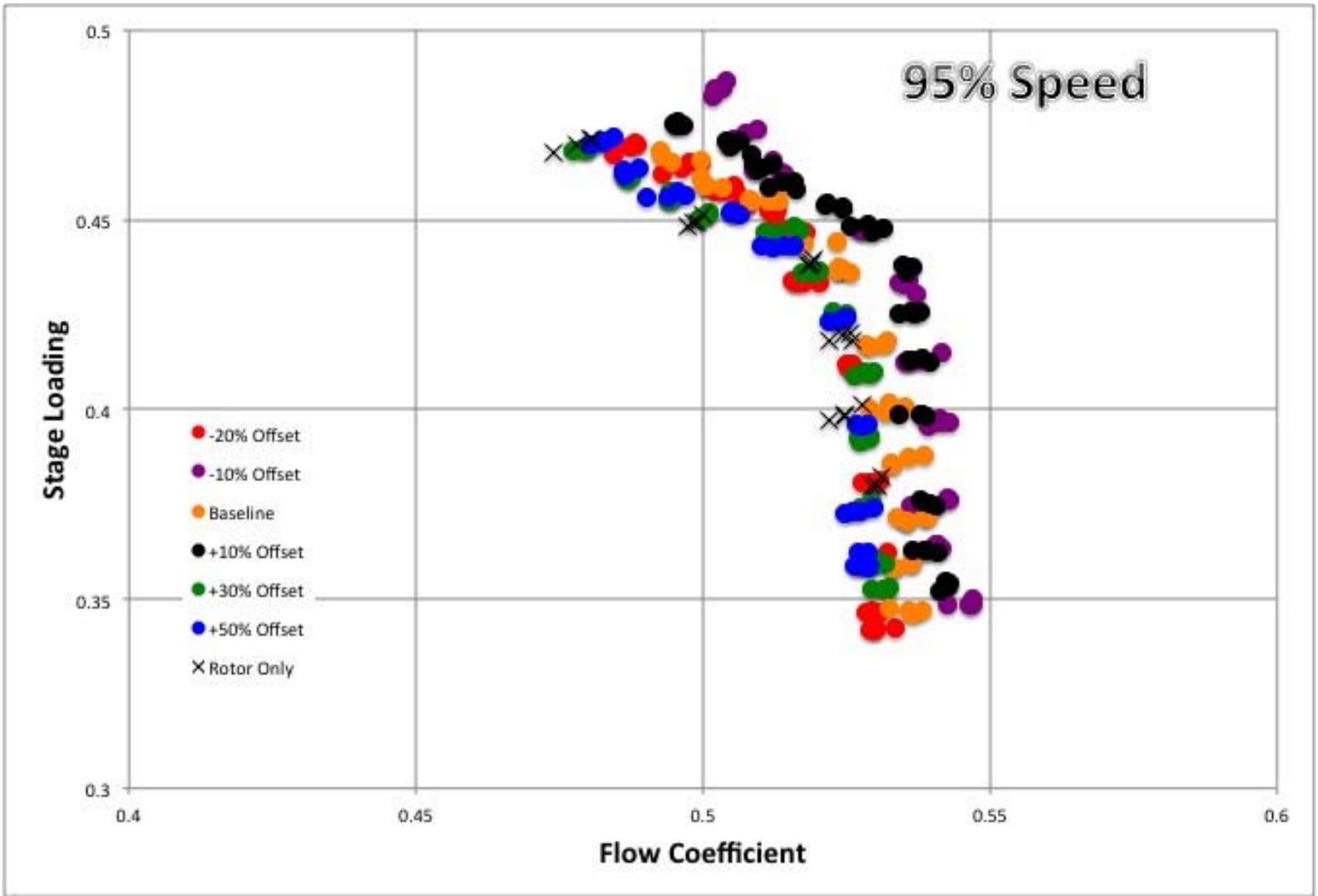
Figure 39. Stage Loading at 95 Percent Speed.
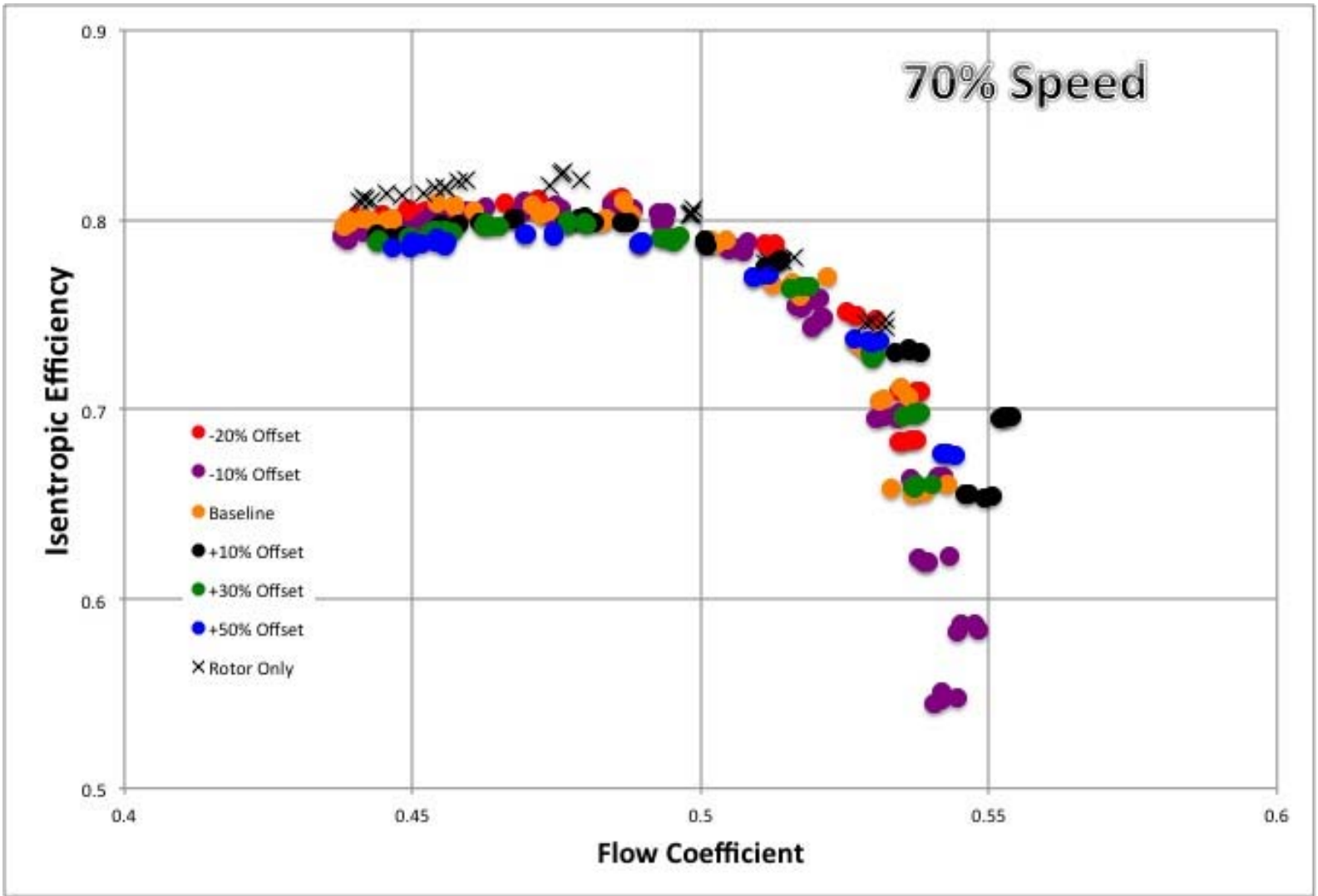
Figure 40. Isentropic Efficiency at 70 Percent Speed.
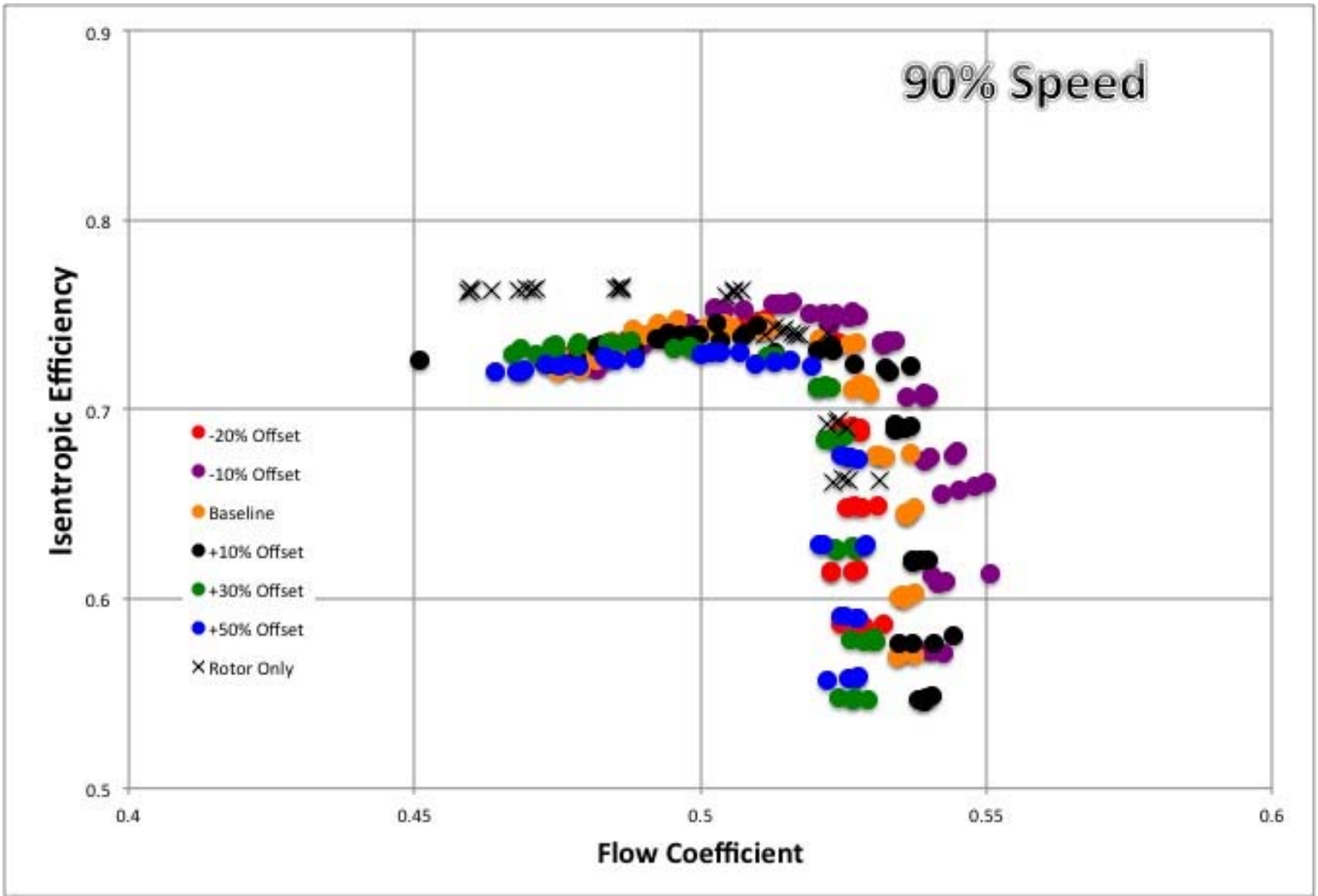
Figure 41. Isentropic Efficiency at 90 Percent Speed.
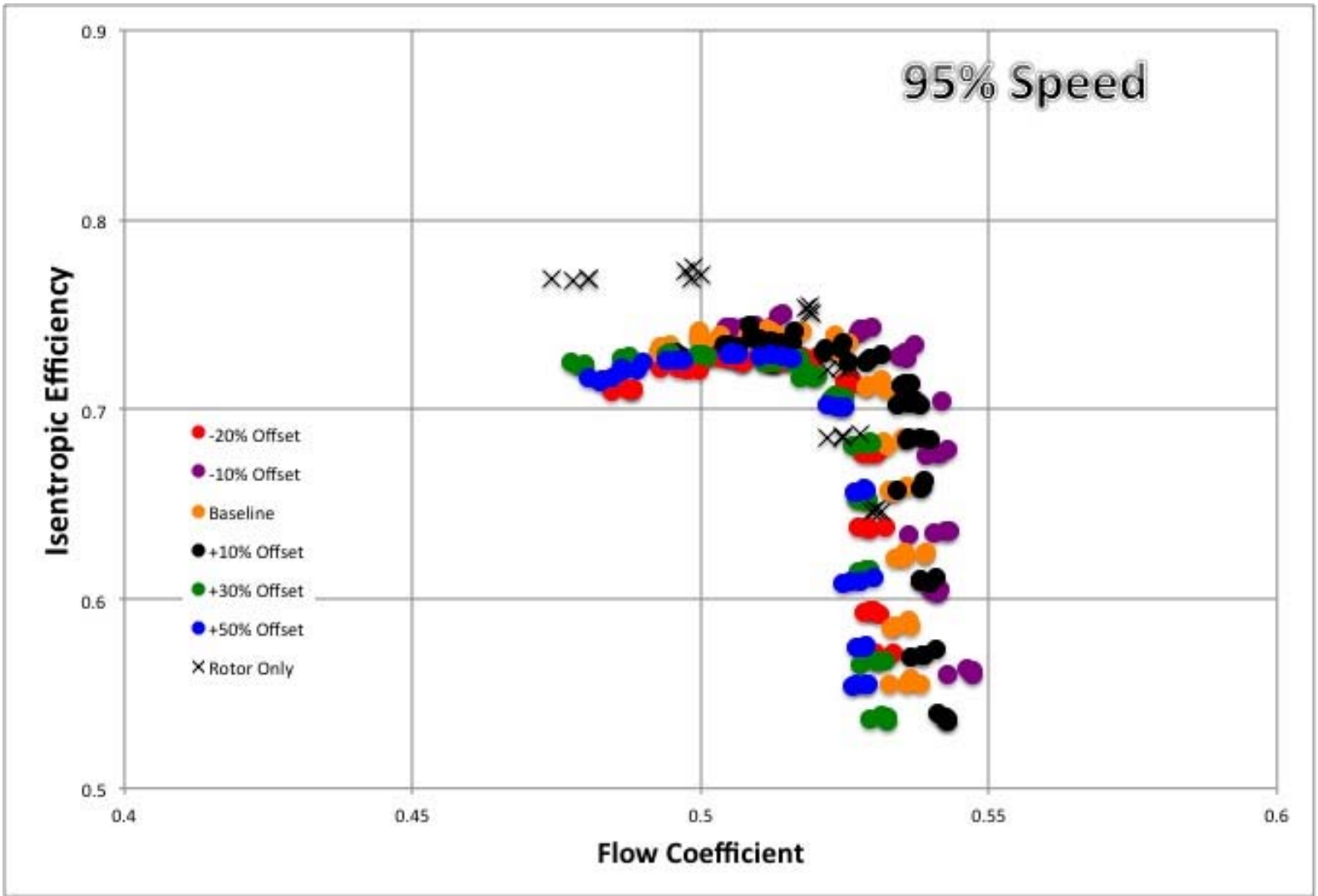
Figure 42. Isentropic Efficiency at 95 Percent Speed.

APPENDIX C. FSI SETUP INSTRUCTIONS IN ANSYS WORKBENCH

These instructions are not all-inclusive and are included as a quick reference to an avid user, familiar with ANSYS. For a more informational set of instructions it is recommended to conduct tutorial 23: Oscillating Plate with Two-Way Fluid-Structure Interaction

1. Set up project and share geometry

2. Set up mechanical model

    a. Material model

    b. Load and constraints

    c. Identify the FSI

3. Set up CFD model

    a. Flow properties and flow boundary conditions

    b. Identify the FSI and specify mesh motion model

4. Set up execution control and solve

    a. Time duration and time steps

    b. Coupling sequence

    c. Number of coupling iterations per time step

    d. Interface exchange under-relaxation and convergence criteria

THIS PAGE INTENTIONALLY LEFT BLANK.

APPENDIX D. COLD SHAPE CFX SETUP REPORT

1. Mesh Report
Table 1. Mesh Information for Fluid

Domain	Nodes	Elements
Default Domain	172507	727349

2. Physics Report
Table 2. Domain Physics for Fluid

Domain - Default Domain	
Type	Fluid
Location	B44
Materials	
Air Ideal Gas	
Fluid Definition	Material Library
Morphology	Continuous Fluid
Settings	
Buoyancy Model	Non Buoyant
Domain Motion	Rotating
Angular Velocity	-1.8900e+04 [rev min^-1]
Axis Definition	Coordinate Axis
Rotation Axis	Coord 0.1
Mesh Deformation	Regions of Motion Specified
Displacement Relative To	Previous Mesh
Mesh Motion Model	Displacement Diffusion
Mesh Stiffness	Increase near Small Volumes
Stiffness Model Exponent	2.0000e+00
Reference Volume	Mean Control Volume
Reference Pressure	1.0000e+00 [atm]
Heat Transfer Model	Total Energy
Include Viscous Work Term	True
Turbulence Model	k epsilon
Turbulent Wall Functions	Scalable
High Speed Model	Off
Domain Interface - RotorSym11	
Boundary List1	RotorSym11 Side 1
Boundary List2	RotorSym11 Side 2
Interface Type	Fluid Fluid
Settings	
Interface Models	Rotational Periodicity
Axis Definition	Coordinate Axis
Rotation Axis	Coord 0.1
Mesh Connection	Automatic

Table 3. Boundary Physics for Fluid

Domain	Boundaries	
Default Domain	**Boundary - Inlet**	
	Type	INLET
	Location	Inlet
	Settings	
	Flow Direction	Normal to Boundary Condition
	Flow Regime	Subsonic
	Heat Transfer	Stationary Frame Total Temperature
	Stationary Frame Total Temperature	2.8815e+02 [K]
	Mass And Momentum	Stationary Frame Total Pressure
	Relative Pressure	0.0000e+00 [Pa]
	Mesh Motion	Stationary
	Turbulence	Medium Intensity and Eddy Viscosity Ratio
	Boundary - RotorSym11 Side 1	
	Type	INTERFACE
	Location	RotorSym1
	Settings	
	Heat Transfer	Conservative Interface Flux
	Mass And Momentum	Conservative Interface Flux
	Mesh Motion	Conservative Interface Flux
	Turbulence	Conservative Interface Flux
	Boundary - RotorSym11 Side 2	
	Type	INTERFACE
	Location	RotorSym2
	Settings	
	Heat Transfer	Conservative Interface Flux
	Mass And Momentum	Conservative Interface Flux
	Mesh Motion	Conservative Interface Flux
	Turbulence	Conservative Interface Flux
	Boundary - Outlet	
	Type	OUTLET
	Location	RotorOut
	Settings	
	Flow Regime	Subsonic
	Mass And Momentum	Average Static Pressure
	Pressure Profile Blend	5.0000e-02
	Relative Pressure	2.0700e-01 [atm]
	Mesh Motion	Stationary
	Pressure Averaging	Average Over Whole Outlet
	Boundary - Casing	

Domain	Boundaries	
	Type	WALL
	Location	RotorCasing
	Settings	
	Heat Transfer	Adiabatic
	Mass And Momentum	No Slip Wall
	Wall Velocity Relative To	Mesh Motion
	Wall Velocity	Counter Rotating Wall
	Mesh Motion	Stationary
	Wall Roughness	Smooth Wall
	Boundary - Default Domain Default	
	Type	WALL
	Location	F50.44
	Settings	
	Heat Transfer	Adiabatic
	Mass And Momentum	No Slip Wall
	Wall Velocity Relative To	Mesh Motion
	Mesh Motion	Stationary
	Wall Roughness	Smooth Wall
	Boundary - MainInterface	
	Type	WALL
	Location	MainInterface
	Settings	
	Heat Transfer	Adiabatic
	Mass And Momentum	No Slip Wall
	Wall Velocity Relative To	Mesh Motion
	Mesh Motion	Stationary
	Wall Roughness	Smooth Wall
	Boundary - SplitterInterface	
	Type	WALL
	Location	SplitterInterface
	Settings	
	Heat Transfer	Adiabatic
	Mass And Momentum	No Slip Wall
	Wall Velocity Relative To	Mesh Motion
	Mesh Motion	Stationary
	Wall Roughness	Smooth Wall

THIS PAGE INTENTIONALLY LEFT BLANK.

APPENDIX E. HOT SHAPE CFX SETUP REPORT

1. Mesh Report

Table 1. Mesh Information for ANSYS

Domain	Nodes	Elements
Default Domain	36374	19840

Table 2. Mesh Information for Fluid

Domain	Nodes	Elements
Default Domain	172507	727349

2. Physics Report

Table 3. Domain Physics for Fluid

Domain - Default Domain	
Type	Fluid
Location	B44
Materials	
Air Ideal Gas	
Fluid Definition	Material Library
Morphology	Continuous Fluid
Settings	
Buoyancy Model	Non Buoyant
Domain Motion	Rotating
Angular Velocity	-1.8900e+04 [rev min^-1]
Axis Definition	Coordinate Axis
Rotation Axis	Coord 0.1
Mesh Deformation	Regions of Motion Specified
Displacement Relative To	Previous Mesh
Mesh Motion Model	Displacement Diffusion
Mesh Stiffness	Increase near Small Volumes
Stiffness Model Exponent	2.0000e+00
Reference Volume	Mean Control Volume
Reference Pressure	1.0000e+00 [atm]
Heat Transfer Model	Total Energy
Include Viscous Work Term	True
Turbulence Model	k epsilon
Turbulent Wall Functions	Scalable
High Speed Model	Off
Domain Interface - RotorSym11	
Boundary List1	RotorSym11 Side 1
Boundary List2	RotorSym11 Side 2
Interface Type	Fluid Fluid
Settings	

Interface Models	Rotational Periodicity
Axis Definition	Coordinate Axis
Rotation Axis	Coord 0.1
Mesh Connection	Automatic

Table 4. Boundary Physics for Fluid

Domain	Boundaries	
Default Domain	**Boundary - Inlet**	
	Type	INLET
	Location	Inlet
	Settings	
	Flow Direction	Normal to Boundary Condition
	Flow Regime	Subsonic
	Heat Transfer	Stationary Frame Total Temperature
	Stationary Frame Total Temperature	2.8815e+02 [K]
	Mass And Momentum	Stationary Frame Total Pressure
	Relative Pressure	0.0000e+00 [Pa]
	Mesh Motion	Stationary
	Turbulence	Medium Intensity and Eddy Viscosity Ratio
	Boundary - RotorSym11 Side 1	
	Type	INTERFACE
	Location	RotorSym1
	Settings	
	Heat Transfer	Conservative Interface Flux
	Mass And Momentum	Conservative Interface Flux
	Mesh Motion	Conservative Interface Flux
	Turbulence	Conservative Interface Flux
	Boundary - RotorSym11 Side 2	
	Type	INTERFACE
	Location	RotorSym2
	Settings	
	Heat Transfer	Conservative Interface Flux
	Mass And Momentum	Conservative Interface Flux
	Mesh Motion	Conservative Interface Flux
	Turbulence	Conservative Interface Flux
	Boundary - Outlet	
	Type	OUTLET
	Location	RotorOut
	Settings	
	Flow Regime	Subsonic
	Mass And Momentum	Average Static Pressure
	Pressure Profile Blend	5.0000e-02

Domain	Boundaries	
	Relative Pressure	2.0500e-01 [atm]
	Mesh Motion	Stationary
	Pressure Averaging	Average Over Whole Outlet
	Boundary - Casing	
	Type	WALL
	Location	RotorCasing
	Settings	
	Heat Transfer	Adiabatic
	Mass And Momentum	No Slip Wall
	Wall Velocity Relative To	Mesh Motion
	Wall Velocity	Counter Rotating Wall
	Mesh Motion	Stationary
	Wall Roughness	Smooth Wall
	Boundary - Default Domain Default	
	Type	WALL
	Location	F50.44
	Settings	
	Heat Transfer	Adiabatic
	Mass And Momentum	No Slip Wall
	Wall Velocity Relative To	Mesh Motion
	Mesh Motion	Stationary
	Wall Roughness	Smooth Wall
	Boundary - MainInterface	
	Type	WALL
	Location	MainInterface
	Settings	
	Heat Transfer	Adiabatic
	Mass And Momentum	No Slip Wall
	Wall Velocity Relative To	Mesh Motion
	Mesh Motion	ANSYS MultiField
	ANSYS Interface	FSIN_1
	Receive from ANSYS	Total Mesh Displacement
	Send to ANSYS	Total Force
	Wall Roughness	Smooth Wall
	Boundary - SplitterInterface	
	Type	WALL
	Location	SplitterInterface
	Settings	
	Heat Transfer	Adiabatic
	Mass And Momentum	No Slip Wall
	Wall Velocity Relative To	Mesh Motion
	Mesh Motion	ANSYS MultiField
	ANSYS Interface	FSIN_2

Domain	Boundaries	
	Receive from ANSYS	Total Mesh Displacement
	Send to ANSYS	Total Force
	Wall Roughness	Smooth Wall

LIST OF REFERENCES

[1]   Wennerstrom A. J., 2000, Design of Highly Loaded Axial-Flow Fans and Compressors, White River Junction, VT: Concepts ETI, Inc.

[2]   Wennerstrom A. J., 1987, "Some Experiments with a Supersonic Axial Compressor Stage," ASME Journal of Turbomachinery, 109(3), p. 388–397.

[3]   Wennerstrom, A. J., and Frost, G. R., 1974, "Design of a Rotor Incorporating Splitter Vanes for a High Pressure Ratio Supersonic Axial Compressor Stage," ARL 74–0110, Aerospace Research Laboratories, Wright-Patterson Air Force Base, OH.

[4]   Drayton, S., 2013, "Design, Test, and Evaluation of a Transonic Axial Compressor Rotor with Splitter Blades," Ph.D. dissertation, Naval Postgraduate School, Monterey, CA.

[5]   Lehrfeld, M., 2013, "Performance Improvements to the Naval Postgraduate School Turbopropulsion Labs Transonic Axially Splittered Rotor," Thesis, Naval Postgraduate School, Monterey, CA.

[6]   Hobson, G. V., (Private Communication), 2016.

[7]   Gannon, A. J., (Private Communication), 2016.

THIS PAGE INTENTIONALLY LEFT BLANK.

INITIAL DISTRIBUTION LIST

1.   Defense Technical Information Center
        Ft. Belvoir, Virginia

2.   Dudley Knox Library
        Naval Postgraduate School
        Monterey, California